Self-propulsion near the onset of Marangoni instability of deformable active droplets

Matvey Morozov[1] and Sébastien Michelin[1,†]

[1]LadHyX – Département de Mécanique, École Polytechnique – CNRS, 91128 Palaiseau CEDEX, France

Experimental observations indicate that chemically active droplets suspended in a surfactant-laden fluid can self-propel spontaneously. The onset of this motion is attributed to a symmetry-breaking Marangoni instability resulting from the nonlinear advective coupling of the distribution of surfactant to the hydrodynamic flow generated by Marangoni stresses at the droplet's surface. Here, we use a weakly nonlinear analysis to characterize the self-propulsion near the instability threshold and the influence of the droplet's deformability. We report that, in the vicinity of the threshold, deformability enhances self-propulsion of viscous droplets, but hinders propulsion of drops that are roughly less viscous than the surrounding fluid. Our asymptotics further reveals that droplet deformability may alter the type of bifurcation leading to symmetry breaking: for moderately deformable droplets, the onset of self-propulsion is transcritical and a regime of steady self-propulsion is stable; while in the case of highly deformable drops, no steady flows can be found within the asymptotic limit considered in this paper, suggesting that the bifurcation is subcritical.

Key words: bifurcation, drops, low-Reynolds-number flows

---

1. Introduction

Several experimental studies have recently reported self-propulsion of active droplets, whose swimming motion in viscous flows arises from spontaneously generated surface tension gradients (Maass *et al.* 2016; Ryazantsev *et al.* 2017). These active droplets can rely on either chemical reactions (Thutupalli, Seemann & Herminghaus 2011) or solubilization (Izri *et al.* 2014; Krüger *et al.* 2016*b*; Moerman *et al.* 2017) as a source of chemical energy to power their self-propulsion for many hours at velocities up to one diameter per second. Experimental observations further indicate that self-propelling microdroplets may exhibit complex dynamical behaviour, including straight, curved or chaotic trajectories (Suga *et al.* 2018). Recent studies have focused specifically on the type of chemical activity (Herminghaus *et al.* 2014; Izri *et al.* 2014; Nagasaka *et al.* 2017), the physical properties of the fluid making up the drop (Krüger *et al.* 2016*b*), the presence of other active droplets (Maass *et al.* 2016; Moerman *et al.* 2017) or geometrical constraints on the droplet's environment (Krüger *et al.* 2016*a*; Jin *et al.* 2018). Sophisticated dynamics paired

† Email address for correspondence: sebastien.michelin@ladhyx.polytechnique.fr

with potential biocompatibility makes active droplets a prime candidate for modelling and engineering of biological systems (Izri *et al.* 2014; Maass *et al.* 2016; Nagasaka *et al.* 2017), as well as for studying and characterizing the collective motion of self-propelled agents.

In order to elucidate the mechanisms responsible for their self-propulsion, their complex individual motion and their interactions, active droplets have also attracted much theoretical and modelling effort. Unlike other currently popular microswimmers, such as bacteria or Janus particles, active droplets do not possess inherent asymmetry and, thus, rely on a symmetry-breaking instability to initiate self-propulsion (Herminghaus *et al.* 2014; Ryazantsev *et al.* 2017; Yoshinaga 2017). In a typical scenario, the instability establishes a concentration or temperature gradient, which produces an uneven stress distribution at the droplet interface, and the droplet may self-propel due to the Marangoni effect. Naturally, spontaneous loss of symmetry calls for a bifurcation analysis: Rednikov, Ryazantsev & Velarde (1994*a*,*b*) developed a weakly nonlinear theory of a self-propelling non-deformable active droplet in the presence of a net buoyancy force. In the limit of small Péclet and Reynolds numbers, Rednikov *et al.* showed that the balance of self-propulsion and buoyancy force spawns multiple regimes of steady propulsion of the droplet featuring different flow patterns within and outside of the propelling drop. In contrast, recent theoretical works assume a finite value of Péclet number to emphasize the role of advection in the symmetry-breaking instability enabling the transport of active droplets; several models sharing the same basic ingredients have been considered, which differ on the exact production mechanism, transport or bulk reactivity of the chemical solute responsible for the Marangoni flows at the heart of the symmetry-breaking instability (Thutupalli *et al.* 2011; Yabunaka, Ohta & Yoshinaga 2012; Yoshinaga *et al.* 2012; Izri *et al.* 2014; Moerman *et al.* 2017). In particular, Yoshinaga *et al.* (2012) adopted a weakly nonlinear approach to the problem and derived amplitude equations governing the droplet dynamics near the onset of self-propulsion in the presence of a linear chemical reaction in the bulk fluid.

Three-dimensional Marangoni flow stirred by an active droplet was considered by Schmitt & Stark (2016), who employed their results to engineer a set-up for guiding active drops with laser light. Dynamics of active drops can also be modelled based on reaction–diffusion equations (Shitara, Hiraiwa & Ohta 2011; Schmitt & Stark 2013). In particular, Shitara *et al.* (2011) investigated the motion of an isolated domain confined in an excitable reaction–diffusion system and demonstrated that there are three basic motions of the domain: straight motion, rotating motion and helical motion. The diffusion–advection–reaction equation-based model developed by Schmitt & Stark (2013) also yields several dynamical regimes: depending on the strength of the Marangoni effect, the droplet may self-propel steadily, spontaneously stop or oscillate. The effect of chemical product that changes the interfacial energy of a droplet and thus affects the symmetry-breaking Marangoni instability was investigated by Yabunaka *et al.* (2012), while Yabunaka & Yoshinaga (2016) recently analysed the hydrodynamic and chemical interactions of two droplets, and their resulting collision dynamics. The interested reader is referred to the recent reviews of Herminghaus *et al.* (2014) and Maass *et al.* (2016) on the self-propulsion of active droplets for a more exhaustive review of both experimental and theoretical work on this topic.

It should be noted that the transport due to Marangoni forces is not exclusive to submerged droplets: the same mobility mechanism applies to swimmers moving along a liquid surface (Würger 2014; Frenkel *et al.* 2018). Self-propulsion enabled by a symmetry-breaking instability was also observed in active particles driven by

diffusiophoresis (Moran & Posner 2017). In particular, Michelin, Lauga & Bartolo (2013) have demonstrated theoretically that the flow around a chemically active isotropic autophoretic particle may lose its stability via symmetry-breaking bifurcation, resulting in self-propulsion of the particle. Together with the chemical activity of the particle or droplet, the advective transport of chemical species by the flow field they generate through Marangoni stresses or phoretic slip velocities is, thus, the key ingredient leading to self-propulsion beyond a certain threshold required to overcome the effect of diffusion. Even below the critical threshold for propulsion, chemical activity and phoretic mobility of the particles were also shown to significantly impact their response to outer flows (e.g. phoretic drag reduction (Yariv & Kaynan 2017)).

Self-propelled droplets and rigid diffusiophoretic particles share many similarities but differ on one key feature, namely the origin of the flow field in response to a concentration gradient. For rigid phoretic particles, the flow stems from non-zero slip velocity at the particle surface in response to a chemical gradient, whereas the mobility of Marangoni droplets is sustained by interfacial stresses (Moran & Posner 2017; Yoshinaga 2017). It should be noted that both mechanisms can be described within the same framework, and in fact coexist in the case of droplets, although phoretic effects are essentially negligible in front of Marangoni forcing except for very viscous droplets (Anderson 1989).

As noted in the opening paragraph, the physics of spontaneous self-propulsion is complex and represents considerable interest. In particular, recent experimental observations of liquid-crystal droplets revealed the coupling between the director field inside the drop and the trajectory of droplet self-propulsion (Krüger *et al.* 2016*b*). The importance of the internal droplet structure was further investigated by Kree, Burada & Zippelius (2017), who developed a theoretical model of self-propulsion of a spherical droplet containing a rigid skeleton. Even in the absence of advection, the geometry of active particles was also shown recently to strongly affect or control the direction and magnitude of propulsion as well as their hydrodynamic signature (Lauga & Michelin 2016; Nourhani & Lammert 2016; Michelin & Lauga 2017; Ibrahim, Golestanian & Liverpool 2018). Shape can also act as a symmetry-breaking mechanism for chemically homogeneous systems (Shklyaev, Brady & Cordova-Figueroa 2014; Michelin & Lauga 2015). Although their Laplace pressure remains typically greater than the hydrodynamic viscous stresses they sustain from the surrounding fluid, self-propelled droplets do not have a fixed shape but may deform under the effect of surfactant gradients or fluid motion. One of the present paper's main objectives is to characterize the fundamental effect of surface deformability on mode competition and self-propulsion characteristics of active droplets. Deformability typically accompanies self-propulsion of microorganisms and active particles in general (Winklbauer 2015; Ohta 2017). The dynamics of deformable droplets driven by the Marangoni effect was recently investigated theoretically by Yoshinaga (2014) and by means of lattice-Boltzmann simulations by Fadda *et al.* (2017).

A large number of microscopic active droplets sustained in a bulk liquid constitute an active emulsion. It has been established that the collective behaviour of drops in active emulsions may follow several distinct scenarios of symmetry breaking (Herminghaus *et al.* 2014). The focus of the present paper is on the self-propulsion of a single active droplet, and such collective phenomena are beyond the scope of the present paper; we refer the reader interested in the theory of active emulsions to the recent review by Weber *et al.* (2018).

Active droplets have typical diameters of a few tens of micrometres, and swim at a few micrometres per second. Hence, viscous stresses are typically much larger

than inertial forces. Following recent theoretical analyses of active droplets (see Herminghaus *et al.* 2014; Izri *et al.* 2014; Yoshinaga 2014; Maass *et al.* 2016), we consider the droplet dynamics within the framework of Stokes flows and for moderate values of the Péclet number. We note that the self-propulsion of an active deformable droplet in the limit of high solutal Péclet number, $Pe \gg 1$, and vanishing thermal Péclet number was investigated by Golovin, Gupalo & Ryazantsev (1989). Unlike Yabunaka *et al.* (2012) and Yoshinaga *et al.* (2012), we disregard any chemical reaction in the bulk fluid both within and outside the droplet. That is, in our model, activity is sustained by a reaction at the droplet interface which roughly corresponds to the micellar dissolution under moderate surfactant concentration (i.e. lower than the critical micelle concentration), as observed by Moerman *et al.* (2017). We adopt an asymptotic approach to the problem at hand to obtain the self-propulsion characteristics near the onset of propulsion as well as analyse the stability of the steady-state solutions. As opposed to the analyses of Rednikov *et al.* (1994*a*,*b*), we include dynamic deformability of the droplet interface into consideration and build our argument based on both the investigation of steady states and explicit stability analysis of these states. The latter allows us to distinguish between physically different temporal scales involved in the onset of the Marangoni instability, thus providing additional insight into the competition of different physical mechanisms driving the droplet dynamics.

The paper is organized as follows. In § 2, the mathematical formulation of the problem is outlined and relevant dimensionless parameters are defined. Neutrally stable eigenmodes of the linearized problem are obtained in § 3. Then § 4 presents a weakly nonlinear analysis of the problem in order to identify and characterize the steady flow regimes emerging due to saturation of neutrally stable modes above the instability threshold. In § 5, linear stability analysis of these steady states is discussed and is employed to estimate the typical time scales associated with saturation of different instability modes. Finally, we discuss our findings in § 6 and present some perspectives.

2. Physical problem and model

The focus of the present work is the spontaneous propulsion and fluid motion generated by active droplets under the effect of the Marangoni instability, and more specifically the effect of interface deformability on the dynamics of an active droplet near the onset of self-propulsion. We focus on an axisymmetric problem and employ spherical polar coordinates $(r, \mu = \cos\theta)$ centred at the droplet's centre of mass.

2.1. *Governing equations and boundary conditions*

A liquid droplet of a Newtonian fluid is considered here, with density ρ_i and dynamic viscosity η_i, submerged in a second Newtonian fluid of density ρ_o and viscosity η_o, containing a surfactant solute of concentration C, as sketched in figure 1. Note that different experimental set-ups employ different inner and outer fluids: for instance, Izri *et al.* (2014) observed water droplets in oil, while others used oil droplets in water (Moerman *et al.* 2017). To remain general, we denote in the following by subscripts i and o the quantities relevant to the inner and outer fluid, respectively. Far from the droplet, the concentration of surfactant molecules is $\mathcal{C}_\infty$. In the following, we consider axisymmetric deformations of the droplet under flow and Marangoni stresses, whose surface is thus described in spherical polar coordinates by $r = R(t, \mu)$ with $\mu = \cos\theta$.
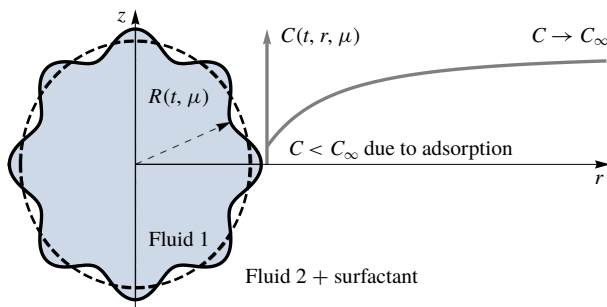
FIGURE 1. (Colour online) Cross-section of an axisymmetric deformable active droplet undergoing gradual micellar dissolution. As the droplet dissolves, it adsorbs surfactant that powers the chemical reaction at the droplet interface, thus sustaining the dissolution.

Denoting the radius of the drop at rest (i.e. when it is spherical) as R_0, the radius of the deformed droplet can be written as

$$R(t, \mu) = R_0(1 + \xi(t, \mu)). \tag{2.1}$$

Naturally, the presence of deformations would contribute not only to the position of the droplet interface, but also to its curvature. That is, vectors normal and tangential to the interface are now functions of t and μ, thus affecting the boundary conditions formulated below.

Multiple physico-chemical mechanisms have been identified in experiments leading to the self-propulsion of active droplets (Herminghaus *et al.* 2014). In the following, we explicitly refer to the molecular pathway identified in the experiments of Moerman *et al.* (2017). Yet the formalism presented here is completely general and could easily be applied to the micellar pathway relevant to the experiments of Izri *et al.* (2014). In the molecular pathway leading to the solubilization of the oil phase into the aqueous solution, surfactant molecules are absorbed at the surface and swollen micelles are released, leading to slow decrease of the droplet size. In experiments, the typical time of droplet dissolution is substantially longer than the time scale associated with self-propulsion (Izri *et al.* 2014; Moerman *et al.* 2017), so that this dissolution process can be neglected and the volume of the droplet is assumed constant, $V = \text{const.}$, while the droplet consumes surfactant molecules at a fixed rate $\mathcal{A} > 0$,

$$\mathcal{D}\boldsymbol{n} \cdot \boldsymbol{\nabla} C = \mathcal{A} \quad \text{at } r = R, \tag{2.2}$$

where $\boldsymbol{n}$ is the outward normal to the droplet interface. Surfactant molecules do not penetrate into the droplet. Thus, advection–diffusion of surfactant should only be taken into account outside of the drop,

$$\partial_t C + \boldsymbol{u}_o \cdot \boldsymbol{\nabla} C = \mathcal{D}\nabla^2 C, \tag{2.3}$$

where ∂_t denotes the partial derivative with respect to time t, $\boldsymbol{u}_o$ is the flow velocity outside of the drop, and $\mathcal{D}$ denotes the molecular diffusivity of the surfactant in the outer fluid. Naturally, far away from the droplet, surfactant concentration reaches a constant value,

$$C \to \mathcal{C}_\infty \quad \text{for } r \to \infty. \tag{2.4}$$

The presence of surfactant at the droplet's surface modifies its interfacial tension γ. Assuming that adsorption/desorption of surfactant molecules at the fluid–fluid interface occurs instantaneously compared to its transport in the outer fluid, the concentration of the adsorbed surfactants is $\propto C|_{r=R}$ (Baret 1969). We further linearize the relationship between γ and $C|_{r=R}$,

$$\gamma = \gamma_0 - \gamma_C (C|_{r=R} - \mathcal{C}_\infty + \mathcal{A}R_0/\mathcal{D}), \qquad (2.5)$$

and note that $\gamma_C \equiv -(\mathrm{d}\gamma/\mathrm{d}C)|_{C=\mathcal{C}_\infty - \mathcal{A}R_0/\mathcal{D}} > 0$ with $\mathcal{C}_\infty - \mathcal{A}R_0/\mathcal{D}$ corresponding to the surfactant concentration at $r = R$ in the absence of flow. The stress balance at the interface can then be written in vector form (i.e. accounting for both normal and tangential stresses) as

$$(\boldsymbol{\sigma}_o - \boldsymbol{\sigma}_i) \cdot \boldsymbol{n} + \boldsymbol{\nabla} \cdot [(\boldsymbol{I} - \boldsymbol{nn})\gamma] = 0 \quad \text{at } r = R, \qquad (2.6)$$

where $\boldsymbol{I}$ is the identity tensor, $\boldsymbol{\sigma}_{i,o} = -P_{i,o}\boldsymbol{I} + \boldsymbol{\tau}_{i,o}$ is the hydrodynamic stress tensor with $\boldsymbol{\tau}_{i,o} = \eta_{i,o}(\boldsymbol{\nabla}\boldsymbol{u}_{i,o} + \boldsymbol{\nabla}\boldsymbol{u}_{i,o}^{\mathrm{T}})$ its viscous part. The continuity of the fluid's velocity and impermeability of the droplet's surface is written as

$$R_0 \frac{\partial \xi}{\partial t} - R_0 \frac{\sqrt{1-\mu^2}}{r} \frac{\partial \xi}{\partial \mu}(\boldsymbol{u}_o \cdot \boldsymbol{e}_\theta) = \boldsymbol{u}_o \cdot \boldsymbol{e}_r, \quad \boldsymbol{u}_o = \boldsymbol{u}_i \quad \text{at } r = R. \qquad (2.7)$$

In experiments, typical droplet sizes and velocities are respectively $R_0 \sim 10$ µm and $V \sim 10$ µm s^{-1} (Izri *et al.* 2014; Moerman *et al.* 2017), so that the Reynolds number $Re = \rho_o V R_0/\eta_o$ is small and inertia can essentially be neglected so that the velocity $\boldsymbol{u}_{i,o}$ and pressure $P_{i,o}$, both inside and outside the droplet, satisfy the Stokes equations

$$\boldsymbol{\nabla} \cdot \boldsymbol{u}_{i,o} = 0, \quad \boldsymbol{\nabla}P_{i,o} = \eta_{i,o}\nabla^2\boldsymbol{u}_{i,o}, \qquad (2.8a,b)$$

with subscripts i and o referring to the inner and outer fluids, respectively. In the reference frame of the droplet's centre considered here, the flow at infinity is opposite to the droplet's translation,

$$\boldsymbol{u} \to -\mathcal{U}_\infty \boldsymbol{e}_z \quad \text{for } r \to \infty, \qquad (2.9)$$

and the system of equations above is closed by enforcing the mechanical equilibrium of the droplet in the absence of inertia, i.e. the force-free condition

$$\int_{r=R} \boldsymbol{\sigma}_o \cdot \boldsymbol{n} \, \mathrm{d}S = \boldsymbol{0}. \qquad (2.10)$$

2.2. *Axisymmetric Stokes flow*

Axisymmetric Stokes flows inside and outside the droplet can be recast in terms of a streamfunction $\psi_{i,o}(t, r, \mu)$, such that

$$\boldsymbol{u} = -\frac{1}{r^2}\frac{\partial \psi}{\partial \mu}\boldsymbol{e}_r - \frac{1}{r\sqrt{1-\mu^2}}\frac{\partial \psi}{\partial r}\boldsymbol{e}_\theta. \qquad (2.11)$$

The general solution of the Stokes equations (2.8) for the inner and outer flows in axisymmetric spherical coordinates is given by a superposition of orthogonal modes, the so-called Lamb solution (Lamb 1945; Happel & Brenner 1983; Leal 2007).

The flow outside the droplet must converge to a finite unidirectional flow as $r \to \infty$, and the flow inside the droplet must be regular at the origin, so the streamfunction and pressure can be written generally in the outer fluid as

$$\psi_o(t, r, \mu) = \left(\frac{a_{o,1}(t)}{r} - b_{o,1}(t)r^2 \right)(1 - \mu^2) + \sum_{n=2}^{\infty} \left(\frac{a_{o,n}(t)}{r^n} - \frac{b_{o,n}(t)}{r^{n-2}} \right)(1 - \mu^2)L'_n(\mu),$$
(2.12)

$$P_o(t, r, \mu) = \eta_o \sum_{n=2}^{\infty} 2n(1 - 2n)b_{o,n}(t)\frac{L_n(\mu)}{r^{n+1}},$$
(2.13)

and within the droplet as

$$\psi_i(t, r, \mu) = \sum_{n=1}^{\infty} (a_{i,n}(t)r^{n+1} - b_{i,n}(t)r^{n+3})(1 - \mu^2)L'_n(\mu),$$
(2.14)

$$P_i(t, r, \mu) = -2\eta_i \sum_{n=0}^{\infty} b_{i,n}(t)(n + 1)(2n + 3)r^n L_n(\mu),$$
(2.15)

where L_n denotes the nth Legendre polynomial and the prime denotes the derivative. Note that the Stokeslet term is omitted in (2.12) since the droplet is force-free (Blake 1971), which effectively enforces (2.10) automatically. The different modes in (2.12) correspond to singularities of increasing order in the hydrodynamic signature of the swimming droplet, and are associated with specific physical characteristics of the self-propulsion and associated fluid motion. For instance, the mode with $n = 1$ carries information about the droplet self-propulsion velocity (since it is the only mode with non-zero velocity as $r \to \infty$), the mode with $n = 2$ corresponds to a symmetric extensile flow akin to the flow excited by a force dipole (i.e. a stresslet), and so on. Note that the inner and outer hydrodynamic problems are fully determined by computing the intensity of the different modes $(a_{n,i}, b_{n,i})$ and $(a_{n,o}, b_{n,o})$, respectively.

2.3. *Non-dimensionalization*

In the following, all quantities are non-dimensionalized using R_0, $\mathcal{A}R_0/\mathcal{D}$ and $R_0/\mathcal{V}$ as reference scales for length, relative concentration of surfactant (i.e. $C - C_\infty$) and time, respectively. Here, $\mathcal{V}$ is the typical Marangoni velocity of a droplet in a surfactant gradient $\mathcal{A}$ (Anderson 1989):

$$\mathcal{V} \equiv \frac{\gamma_C \mathcal{A}R_0}{\mathcal{D}(2\eta_o + 3\eta_i)}.$$
(2.16)

The pressure and viscous stress tensors are further rescaled as

$$P_i \to P_\infty + \frac{2\gamma_0}{R_0} + \frac{\eta_o \mathcal{V}}{R_0}\eta P_i, \quad P_o \to P_\infty + \frac{\eta_o \mathcal{V}}{R_0}P_o, \quad (\boldsymbol{\tau}_i, \boldsymbol{\tau}_o) \to \frac{\eta_o \mathcal{V}}{R_0}(\eta \boldsymbol{\tau}_i, \boldsymbol{\tau}_o),$$
(2.17a−c)

where P_∞ is the constant background pressure, γ_0 the surface tension of the same spherical droplet in the absence of flow, and $\eta \equiv \eta_i/\eta_o$ is the viscosity ratio. We further denote by $U_\infty \equiv \mathcal{U}_\infty/\mathcal{V}$ the swimming velocity of the droplet. Besides η, the physical

problem is entirely characterized by two additional non-dimensional parameters, the Péclet and capillary numbers,

$$Pe \equiv \frac{\mathcal{V}R_0}{\mathcal{D}}, \quad Ca \equiv \frac{\gamma_C \mathcal{A} R_0}{\mathcal{D}\gamma_0}, \quad (2.18a,b)$$

that characterize the relative magnitude of surfactant advection and diffusion, and the relative magnitude of Marangoni and Laplace stresses, respectively.

2.4. *Isotropic motionless base state*

Equations (2.1)–(2.10) feature a motionless isotropic steady state given by

$$\bar{\xi} = 0, \quad \bar{\boldsymbol{u}}_i = \bar{\boldsymbol{u}}_o = \boldsymbol{0}, \quad \bar{P}_i = \bar{P}_o = 0, \quad \bar{C} = -1/r. \quad (2.19a-d)$$

Note that this solution (2.19) exists for any values of *Pe*, *Ca* and η; it features an isotropic surfactant distribution, no Marangoni stresses and, therefore, no droplet motion. In the following, we are interested in the existence and stability of additional non-isotropic steady states emerging in the vicinity of the base state (2.19). This amounts mathematically to finding the fundamental eigenmodes of the system. The next section focuses on finding these eigenmodes and their existence condition (i.e. the corresponding value of *Pe* for given *Ca* and η), while in § 4 we investigate the steady flows sustained by nonlinear saturation of the eigenmodes. Finally, § 5 analyses the stability of the trivial state (2.19) – the stability of the non-isotropic steady state is presented in appendix B.

3. Neutrally stable eigenmodes of the linearized problem

We now carry out a linear analysis of the problem stated in § 2. Specifically, the dimensionless form of the problem formulated in (2.1)–(2.10) is linearized about the base state (2.19) in the case of a steady flow (i.e. $\partial/\partial t = 0$). The solution of the resulting linear problem constitutes a linear stability analysis of the base state in the limit of vanishing perturbation growth rates. By definition, perturbation growth rates vanish at the threshold of monotonic instability. Therefore, solution of the linearized problem allows us to (i) identify the instability threshold and (ii) obtain the set of neutrally stable eigenmodes. At the next stage of analysis, these eigenmodes are used to construct the steady flows emerging above the instability threshold (§ 4).

3.1. *Linearized equations*

The linearized advection–diffusion equation reads

$$\nabla^2 C^{(1)} = -\frac{Pe}{r^4} \frac{\partial \psi_o^{(1)}}{\partial \mu}, \quad (3.1)$$

and linearized boundary conditions at the droplet interface can be written using domain perturbation, i.e. $f|_{r=R} \approx f|_{r=1} + \xi f'|_{r=1}$, as

$$\frac{\partial C^{(1)}}{\partial r} - 2\xi^{(1)} = 0, \quad \psi_i^{(1)} = \psi_o^{(1)} = 0, \quad \frac{\partial \psi_i^{(1)}}{\partial r} = \frac{\partial \psi_o^{(1)}}{\partial r}, \quad (3.2a-c)$$

$$\left(\frac{\partial^2}{\partial r^2} - 2\frac{\partial}{\partial r} - (1-\mu^2)\frac{\partial^2}{\partial \mu^2}\right)(\psi_o^{(1)} - \eta\psi_i^{(1)}) = (2+3\eta)(1-\mu^2)\frac{\partial}{\partial \mu}(C^{(1)} + \xi^{(1)}),$$

$$(3.3)$$

$$\frac{Ca}{2+3\eta}\left[-\eta P_i^{(1)} + P_o^{(1)} + 2\left(\frac{\partial}{\partial r\partial\mu} - 2\frac{\partial}{\partial\mu}\right)(\psi_o^{(1)} - \eta\psi_i^{(1)})\right.$$

$$\left. - 2(2+3\eta)(C^{(1)} - 2\xi^{(1)})\right] = 2\xi^{(1)} - 2\mu\frac{\partial\xi^{(1)}}{\partial\mu} + (1-\mu^2)\frac{\partial^2\xi^{(1)}}{\partial\mu^2}, \qquad (3.4)$$

where superscript (1) denotes small perturbations of the base state. Because of the linearity of the Stokes equations, $\psi_{i,o}^{(1)}$ and $P_{i,o}^{(1)}$ assume the same form as (2.12)–(2.15).

The streamfunction and pressure fields can be decomposed into orthogonal modes (2.12)–(2.15). The form of the linearized equations (3.1)–(3.4) suggests that the linearized concentration $C^{(1)}(r,\mu)$ and displacement $\xi^{(1)}(\mu)$ also decompose in orthogonal modes of the form

$$C^{(1)}(r,\mu) = \sum_{n=0}^{\infty} C_n^{(1)}(r)L_n(\mu), \quad \xi^{(1)}(\mu) = \xi_0^{(1)} + \sum_{n=2}^{\infty} \xi_n^{(1)}L_n(\mu), \qquad (3.5a,b)$$

where the radial part of the basis functions of the concentration field $C_n^{(1)}(r)$ and constant amplitudes $\xi_n^{(1)}$, together with the coefficients $(a_{n,i}^{(1)}, b_{n,o}^{(1)}, b_{n,i}^{(1)}, a_{n,o}^{(1)})$ are to be determined below and characterize each orthogonal eigenmode. In the expansion of $\xi^{(1)}(\mu)$ presented in (3.5), we deliberately ignore the term $\propto L_1(\mu)$, since in the limit of small deformations this term corresponds to translation of the droplet, rather than deformation.

3.2. *Asymptotic structure of the concentration field*

Substitution of (2.12) and (3.5) into (3.1) yields an equation for $C_n^{(1)}(r)$ admitting the following solution:

$$C_0^{(1)}(r) = \frac{c_0^{(1)}}{r} + d_0^{(1)}, \quad C_1^{(1)}(r) = \frac{c_1^{(1)}}{r^2} + d_1^{(1)}r + Pe\frac{a_{o,1}^{(1)} + 2b_{o,1}^{(1)}r^3}{2r^3}, \qquad (3.6a,b)$$

$$C_n^{(1)}(r)\Big|_{n>1} = \frac{c_n^{(1)}}{r^{n+1}} + d_n^{(1)}r^n + Pe\frac{na_{o,n}^{(1)} + (n+1)b_{o,n}^{(1)}r^2}{2r^{n+2}}, \qquad (3.7)$$

where $c_n^{(1)}$ and $d_n^{(1)}$ are unknown constants. In the case of a self-propelling drop (i.e. $b_{o,1}^{(1)} \neq 0$), this solution explicitly violates the far-field boundary condition (2.9). This is a well-known feature of advection–diffusion problems in the presence of a weak advective far-field flow: Acrivos & Taylor (1962) used matching asymptotic expansions to demonstrate that perturbations of the solute concentration field due to particle motion are dissipated in a boundary layer located at $r \sim 1/\epsilon \gg 1$, where $0 < \epsilon \ll 1$ quantifies the velocity of the particle with respect to the surrounding fluid. This framework applies here, since asymptotically small perturbations of a motionless base state are considered, and we thus aim to construct a composite solution for the concentration field consisting of two parts: (i) a near-field part, corresponding to the immediate surroundings of the drop, $r \sim 1$,

$$C(r,\mu) = -1/r + \epsilon C^{(1)} + \epsilon^2 C^{(2)} + \cdots, \qquad (3.8)$$

and (ii) a far-field part valid away from the drop, $\rho \equiv r/\epsilon \sim 1 \ (r \gg 1)$,

$$H(\rho,\mu) = \epsilon H^{(1)} + \epsilon^2 H^{(2)} + \cdots, \qquad (3.9)$$
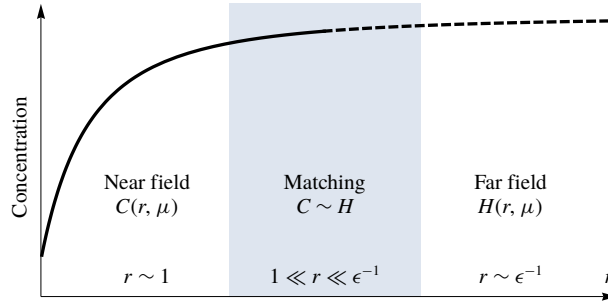
FIGURE 2. (Colour online) Asymptotic structure of the surfactant concentration field around the droplet. The near-field solution $C(r, \mu)$ is matched with the far-field solution $H(r, \mu)$ in the intermediate region where $1 \ll r \ll \epsilon^{-1}$.

as shown in figure 2. Here $H(\rho, \mu)$ satisfies the rescaled advection–diffusion equation, namely,

$$-\epsilon Pe \left(\frac{\partial \psi_o}{\partial \mu} \frac{\partial H}{\partial \rho} - \frac{\partial \psi_o}{\partial \rho} \frac{\partial H}{\partial \mu} \right) = \frac{\partial}{\partial \rho} \left(\rho^2 \frac{\partial H}{\partial \rho} \right) + \frac{\partial}{\partial \mu} \left((1 - \mu^2) \frac{\partial H}{\partial \mu} \right). \quad (3.10)$$

Here ϵ is a small parameter that quantifies the distance to the isotropic steady state. Similarly to the work of Acrivos & Taylor (1962), $C(r, \mu)$ encapsulates the dynamics of the droplet interface, whereas $H(\rho, \mu)$ is determined by advection of the concentration disturbances imparted by the droplet. Naturally, $C(r, \mu)$ and $H(\rho, \mu)$ must yield identical results in the matching region occurring at $1 \ll r \ll 1/\epsilon$ (or, equivalently, $\epsilon \ll \rho \ll 1$) (Holmes 1995). Note that although (3.8) and (3.9) include higher-order terms in ϵ, only $C^{(1)}$ and $H^{(1)}$ are relevant in the context of linear analysis.

3.3. *Concentration field far from the translating drop and asymptotic matching*

Linearization of the rescaled advection–diffusion equation (3.10) about the base state, namely, about $\bar{H} = 0$, yields

$$F(H^{(1)}) \equiv 2Pe\, b_{o,1}^{(1)} \left(\mu \frac{\partial H^{(1)}}{\partial \rho} + \frac{1 - \mu^2}{\rho} \frac{\partial H^{(1)}}{\partial \mu} \right)$$
$$+ \frac{1}{\rho^2} \left[\frac{\partial}{\partial \rho} \left(\rho^2 \frac{\partial H}{\partial \rho} \right) + \frac{\partial}{\partial \mu} \left((1 - \mu^2) \frac{\partial H}{\partial \mu} \right) \right] = 0. \quad (3.11)$$

Its solution that decays as $\rho \to \infty$ can be written as (Acrivos & Taylor 1962)

$$H^{(1)}(\rho, \mu) = \frac{e^{-\rho_s \mu}}{\sqrt{|\rho_s|}} \sum_{n=0}^{\infty} h_n^{(1)} K_{n+1/2}(|\rho_s|) L_n(\mu), \quad (3.12)$$

where $h_n^{(1)}$ are unknown constants to be determined in the matching process with the inner solution, $\rho_s \equiv Pe\, b_{o,1}^{(1)} \rho$, and $K_n(x)$ denotes the modified Bessel function of the second kind of order n. We note that the direction of the droplet motion along the symmetry axis is determined by the sign of the constant amplitude $b_{o,1}^{(1)}$. Since there

is no physical difference between the two directions of motion, we assume $b_{o,1}^{(1)} \geqslant 0$ in what follows.

We use Van Dyke's matching rule (Holmes 1995) to match solutions (3.6), (3.7) and (3.12) in the region $\epsilon \ll \rho \ll 1$. More specifically, $C(r, \mu)$ is expressed in terms of ρ and both C and H are expanded in powers of $\rho \ll 1$. Note that only the terms linear in ϵ, ρ or ϵ/ρ can be matched at the leading order of expansion. As a consequence,

$$d_0^{(1)} = Pe\, b_{o,1}^{(1)}, \quad h_0^{(1)} = -\sqrt{\frac{2}{\pi}}\, Pe\, b_{o,1}^{(1)}, \quad d_n^{(1)} = h_n^{(1)} = 0 \quad \text{for } n > 0. \quad (3.13a\text{--}c)$$

3.4. *Solvability condition*

Substitution of $\psi_i^{(1)}$, $\psi_o^{(1)}$ and $C^{(1)}$ given by (2.12), (2.14), (3.6) and (3.7) into the boundary conditions (3.2)–(3.4) and subsequent projection of the result onto the nth Legendre polynomial yields a sequence of sets of homogeneous linear algebraic equations for the amplitudes $a_{i,n}^{(1)}$, $b_{i,n}^{(1)}$, $a_{o,n}^{(1)}$, $b_{o,n}^{(1)}$, $c_n^{(1)}$ and $\xi_n^{(1)}$. For given n, the solvability condition, i.e. the existence condition for a non-trivial solution to the linearized problem, reads

$$Pe = Pe_n \equiv \begin{cases} 4, & n = 1, \\ \dfrac{4}{2 + 3\eta} \left[(n+1)(2n+1)(1+\eta) - Ca \left(1 + \eta \dfrac{n-1}{n+2}\right) \right], & n > 1. \end{cases} \quad (3.14)$$

Equations (3.14) determine when the linearized problem yields a non-trivial time-independent (i.e. neutrally stable) solution. In §5, we will show that Pe_n is the minimum Péclet number below (respectively above) which the isotropic state is linearly stable (respectively unstable) to perturbations along the nth mode presented above. In other words, Pe_n represents the threshold of the nth mode of monotonic instability. This motivates referring to Pe_n as the instability threshold for mode n in the following. Depending on the value of the capillary number Ca, one of the first two modes in (3.14) features the lowest instability threshold. As a consequence, the next stages of the analysis are focused exclusively on these first two instability modes, namely, the cases of $n = 1$ and $n = 2$, shown in figure 3.

The first eigenmode ($n = 1$, $Pe_1 = 4$) reads

$$b_{i,0}^{(1)} = \frac{Pe_1 A_1}{3\eta}(2 + 3\eta), \quad \frac{3}{2} a_{i,1}^{(1)} = \frac{3}{2} b_{i,1}^{(1)} = a_{o,1}^{(1)} = b_{o,1}^{(1)} = A_1, \quad (3.15a,b)$$

$$c_0^{(1)} = 0, \quad d_0^{(1)} = Pe_1 A_1, \quad c_1^{(1)} = -\frac{3Pe_1 A_1}{4}, \quad d_1^{(1)} = 0, \quad (3.16a\text{--}d)$$

and physically corresponds to a polar concentration field at the surface of the droplet $C^{(1)} \propto \mu$, which maintains its steady translation. The corresponding flow field is that of a translating droplet, i.e. the superposition of a steady flow with a source dipole singularity to enforce the impermeability condition. Note that the instability threshold $Pe_1 = 4$ does not include the viscosity ratio η, since we define dimensionless velocity based on the terminal velocity of a droplet in an imposed gradient of surfactant concentration (2.16) (Anderson 1989).
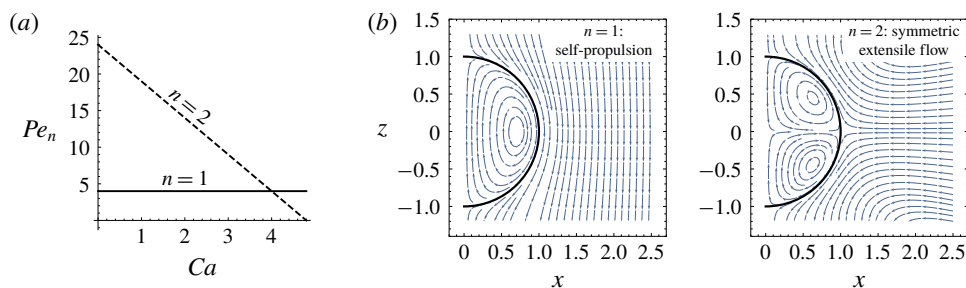
FIGURE 3. (Colour online) Two instability modes competing for the minimal value of the instability threshold Pe_n. (*a*) Evolution of the critical Péclet number with the capillary number for $\eta = 1$. (*b*) Flow field corresponding to the first and the second mode of instability, respectively.

The second eigenmode ($n = 2$) can be written as

$$a_{i,2}^{(1)} = b_{i,2}^{(1)} = a_{o,2}^{(1)} = b_{o,2}^{(1)} = A_2, \quad \xi_2^{(1)} = Ca\, A_2 \frac{4 + \eta}{2(2 + 3\eta)}, \qquad (3.17a,b)$$

$$c_2^{(1)} = -\frac{A_2}{3} \left(7Pe_2 + Ca \frac{4 + \eta}{2 + 3\eta} \right), \quad d_2^{(1)} = 0. \qquad (3.18a,b)$$

In that case, the concentration field $C^{(1)} \propto L_2(\mu)$ is front–back symmetric and cannot drive any net droplet motion. Instead, an extensile flow is forced by the Marangoni stress. Outside the droplet, it takes the same form as the second mode of the classical squirmer model (Blake 1971) and consists of a stresslet singularity (i.e. symmetric force dipole) and source quadrupole.

The amplitudes of the eigenmodes of the system, $A_1 \geqslant 0$ in (3.15), (3.16) or A_2 in (3.17), (3.18), remain naturally undetermined within this linear framework. The weakly nonlinear analysis, which is the focus of the next section, will provide these saturation amplitudes in the vicinity of the critical conditions $Pe = Pe_n$.

Finally, we note that (3.14) echoes the result of the stability analysis in the case of chemically active isotropic particles developed by Michelin *et al.* (2013). In particular, Michelin *et al.* have demonstrated that the onset of spontaneous self-propulsion of active spherical particles also corresponds to $Pe = 4$. We argue that the persisting value of the instability threshold is related to the choice of dimensionless velocity. Both this paper and the work of Michelin *et al.* (2013) define dimensionless velocity based on the velocity of an active drop/particle in an external concentration gradient $\mathcal{A}/\mathcal{D}$. In both cases, self-propulsion and the resulting advection of the concentration field generates a front–back concentration contrast. The onset of the drop or particle motion then corresponds in both cases to a fixed ratio of advective (i.e. destabilizing) and diffusive (i.e. stabilizing) terms, resulting in a fixed value of the Péclet number, $Pe = 4$.

4. Weakly nonlinear analysis

Each of the neutrally stable eigenmodes obtained in §3 exists at a distinct value of Pe given by (3.14). To determine the saturation properties of the eigenmodes, we now successively analyse the behaviour of the different modes near the corresponding

critical Péclet number. Formally speaking, higher-order terms of the asymptotic expansion established in (3.8) and (3.9) are now included to investigate whether nonlinear terms allow for the saturation of growing perturbations, thus enabling a steady flow. Below, we focus specifically on the first two modes (which present the lowest critical Péclet number) and demonstrate that the two competing modes of instability shown in figure 3 spawn two families of steady flows.

To study the nonlinear behaviour of the neutral modes shown in figure 3, we assume that the Péclet number is close to the corresponding critical value,

$$Pe = Pe_n + \epsilon\delta, \tag{4.1}$$

where $\epsilon\delta$ measures the distance to the critical Péclet number and $\delta = O(1)$. The concentration field is expanded as in (3.8) and (3.9), whereas the flow field and droplet shape are expanded near the isotropic steady state as

$$(\psi_i, \psi_o, \xi) = \epsilon(\psi_i^{(1)}, \psi_o^{(1)}, \xi^{(1)}) + \epsilon^2(\psi_i^{(2)}, \psi_o^{(2)}, \xi^{(2)}) + \cdots. \tag{4.2}$$

At each order, approximation $\xi^{(j)}$ is given by a superposition of Legendre polynomials, as shown in (3.5), and the streamfunctions are expanded as in (2.12) and (2.14). Substituting the expansions (3.8), (3.9), (4.1) and (4.2) into the dimensionless form of (2.2)–(2.10), a sequence of problems is obtained at successive orders of ϵ. The first problem in the sequence comprises $O(\epsilon)$ terms and is identical to the linearized problem considered in § 3. The rest of this section is devoted to the higher-order problems in ϵ.

4.1. *Steady self-propulsion* ($n = 1$)

In the case of $n = 1$, $Pe_1 \equiv 4$ and the leading-order flow is given by the first squirming mode with coefficients presented in (3.15) and (3.16). This squirming mode corresponds to a self-propelling droplet and, to determine the self-propulsion velocity, we now consider the problem at ϵ^2 featuring quadratic interactions of the flow and concentration fields obtained at ϵ.

4.1.1. *Concentration field around the droplet*

The quadratic approximation of the advection–diffusion equation (i.e. retaining only $O(\epsilon^2)$ terms) reads

$$-Pe_n\frac{1}{r^4}\frac{\partial\psi_o^{(2)}}{\partial\mu} - \nabla^2 C^{(2)} = \frac{Pe_n}{r^2}\left(\frac{\partial\psi_o^{(1)}}{\partial\mu}\frac{\partial C^{(1)}}{\partial r} - \frac{\partial\psi_o^{(1)}}{\partial r}\frac{\partial C^{(1)}}{\partial\mu}\right) + \frac{\delta}{r^4}\frac{\partial\psi_o^{(1)}}{\partial\mu}. \tag{4.3}$$

Using (3.15), (3.16) and the resulting forms of $C^{(1)}$ and $\psi_{i,o}^{(1)}$, the inhomogeneous right-hand side of (4.3) includes non-zero projections onto the zeroth, first and second Legendre harmonics. Accordingly, the angular component of $C^{(2)}(r, \mu)$ is given by the first three Legendre polynomials, namely, $C^{(2)}(r, \mu) = \sum_{n=0}^{2} C_n^{(2)}(r)L_n(\mu)$, with

$$C_0^{(2)}(r) = \frac{c_0^{(2)}}{r} + d_0^{(2)} - Pe_1^2 A_1^2 \frac{8 - 15r + 20r^3 + 80r^6}{120r^5}, \tag{4.4}$$

$$C_1^{(2)}(r) = \frac{c_1^{(2)}}{r^2} + d_1^{(2)}r + \delta A_1\frac{1 + 2r^3}{2r^3} + Pe_1\frac{a_{o,1}^{(2)} + 2b_{o,1}^{(2)}r^3}{2r^3}, \tag{4.5}$$

$$C_2^{(2)}(r) = \frac{c_2^{(2)}}{r^3} + d_2^{(2)} r^2 + Pe_1 \frac{2a_{o,2}^{(2)} + 3b_{o,2}^{(2)} r^2}{2r^4} - Pe_1^2 A_1^2 \frac{10 - 21r + 70r^3 - 42r^4 + 28r^6}{84r^5},$$
(4.6)

where $c_n^{(2)}$ and $d_n^{(2)}$ are unknown constant amplitudes to be determined in the matching process with the far-field boundary layer.

Equation (3.10) reads at $O(\epsilon^2)$ as

$$F(H^{(2)}) = -2(Pe_1 b_{o,1}^{(2)} + \delta A_1) \left(\mu \frac{\partial H^{(1)}}{\partial \rho} + \frac{1 - \mu^2}{\rho} \frac{\partial H^{(1)}}{\partial \mu} \right),$$
(4.7)

where the linear operator F is defined in (3.11). Since $A_1 \geqslant 0$, the solution of (4.7) which decays as $\rho \to \infty$ reads

$$H^{(2)}(\rho, \mu) = \frac{Pe_1 b_{o,1}^{(2)} + \delta A_1}{2} \left(2(1 + \mu) + 3\mu \frac{1 + \rho_s}{\rho_s^2} \right) e^{-\rho_s(1+\mu)}$$
$$+ \frac{e^{-\rho_s \mu}}{\sqrt{\rho_s}} \sum_{n=0}^{\infty} h_n^{(2)} K_{n+1/2}(\rho_s) L_n(\mu),$$
(4.8)

where $h_n^{(2)}$ are unknown constant amplitudes to be determined in the matching process, and $\rho_s \equiv Pe_1 A_1 \rho \geqslant 0$.

Asymptotic matching of $C(r, \mu)$ and $H(r, \mu)$ at $O(\epsilon^2)$ in the region $\epsilon \ll \rho \ll 1$ is achieved by expressing $C(r, \mu) = -1/r + \epsilon C^{(1)} + \epsilon^2 C^{(2)}$ in terms of ρ, and expanding both $C(\rho, \mu)$ and $H(\rho, \mu)$ in powers of ρ. Linear and quadratic terms in ϵ, ρ or ϵ/ρ must now be matched, leading to

$$d_0^{(2)} = Pe_1 b_{o,1}^{(2)} + \delta A_1, \quad d_1^{(2)} = -Pe_1^2 A_1^2, \quad d_n^{(2)} = 0 \quad \text{for } n > 1, \qquad (4.9a\text{--}c)$$

$$h_1^{(2)} = -3 \frac{Pe_1 b_{o,1}^{(2)} + \delta A_1}{\sqrt{2\pi}}, \quad h_n^{(2)} = 0 \quad \text{for } n \neq 1. \qquad (4.10a,b)$$

4.1.2. *Solvability condition*

Combination of (4.9) and (4.4)–(4.6) yields $C^{(2)}(r, \mu)$. Expanding the boundary conditions (2.2), (2.6) and (2.7) at $O(\epsilon^2)$ and projecting the result onto the first three Legendre polynomials provides a set of inhomogeneous linear algebraic equations for the amplitudes $a_{i,n}^{(2)}$, $b_{i,n}^{(2)}$, $a_{o,n}^{(2)}$, $b_{o,n}^{(2)}$, $c_n^{(2)}$ and $\xi_n^{(2)}$. The solvability condition of this set of equations reads

$$A_1(\delta - 32A_1) = 0. \tag{4.11}$$

Equation (4.11) implies that two branches of steady solutions of the nonlinear problem (2.3)–(2.10) exist near Pe_1: the first branch, given by $A_1 = 0$, corresponds to a motionless droplet and is in fact simply the isotropic steady state (2.19) already discussed; the second branch describes a self-propelling drop with finite velocity ($A_1 = \delta/32 > 0$). Note that in the case of self-propulsion, the velocity of the droplet grows linearly with $Pe - Pe_1$ (i.e. $A_1 \propto \delta$), suggesting that the onset of the droplet motion is a transcritical bifurcation. Also recall that the self-propelling mode is associated with no droplet deformation. As a result, the solvability condition (4.11) does not include Ca, i.e. in the leading order, deformability does not affect droplet self-propulsion velocity.

Following the steps of the analysis above, it is easy to demonstrate that, in the case of $A_1 \leqslant 0$, the counterpart of the solvability condition (4.11) reads

$$A_1(\delta + 32A_1) = 0, \qquad (4.12)$$

implying that, similarly to the case of $A_1 \geqslant 0$, the steady problem is solvable either for $A_1 = 0$ or for $\delta > 0$, i.e. above the threshold of the Marangoni instability.

4.1.3. *Effect of deformability on the droplet's self-propulsion*

Equation (4.11) provides the leading-order evolution of the droplet velocity for the self-propelled steady state near the onset of propulsion, $Pe = Pe_1$, and was obtained by considering the solvability condition of the problem including corrections up to $O(\epsilon^2)$. We now use the same approach to extend the expansion of the different equations up to $O(\epsilon^3)$ and obtain the quadratic correction for the self-propulsion velocity.

When the solvability condition (4.11) is satisfied, the non-trivial solution of the problem at $O(\epsilon^2)$ can be written as

$$b_{i,0}^{(2)} = \frac{(2+3\eta)(29\delta^2 + 10240B_1)}{7680\eta}, \quad \frac{3}{2}a_{i,1}^{(2)} = \frac{3}{2}b_{i,1}^{(2)} = a_{o,1}^{(2)} = b_{o,1}^{(2)} = B_1, \quad (4.13a,b)$$

$$a_{i,2}^{(2)} = b_{i,2}^{(2)} = a_{o,2}^{(2)} = b_{o,2}^{(2)} = -\frac{33\delta^2}{896(Pe_2 - 4)}, \quad \xi_2^{(2)} = -\frac{33Ca\delta^2(4+\eta)}{1792(2+3\eta)(Pe_2 - 4)},$$
$$(4.14a,b)$$

$$c_0^{(2)} = -\frac{\delta^2}{128}, \quad d_0^{(2)} = 4B_1 + \frac{\delta^2}{32}, \quad c_1^{(2)} = -\left(\frac{\delta^2}{32} + 3B_1\right), \quad d_1^{(2)} = -\frac{\delta^2}{64},$$
$$(4.15a-d)$$

$$c_2^{(2)} = 3\delta^2 \frac{20(12+17\eta) + 3Ca(4+\eta)}{896(2+3\eta)(Pe_2 - 4)}, \quad d_2^{(2)} = 0, \qquad (4.16a,b)$$

where the remaining unknown constant B_1 is determined from the solvability condition at $O(\epsilon^3)$. It should be noted in (4.13)–(4.16) that the leading-order deformation of the self-propelling droplet is $O(\epsilon^2)$ (recall that $\xi^{(1)} = 0$) and always corresponds to an oblate shape ($\xi_2^{(2)} < 0$). The leading-order volume change is $O(\epsilon^4)$, so that volume conservation is automatically enforced up to quartic order in ϵ.

To obtain a correction to the droplet self-propulsion velocity, the weakly nonlinear analysis must be carried out up to the cubic order. The solution procedure of the problem at ϵ^3 remains exactly the same as for the lower-order problems, and several intermediate results of the derivation are provided in appendix A. As for the ϵ^2 problem, the solvability condition at ϵ^3 provides information about the $O(\epsilon^2)$ droplet velocity, namely,

$$\begin{aligned} U_\infty &= 2(\epsilon A_1 + \epsilon^2 B_1) \\ &= \frac{Pe - 4}{16} \\ &\quad - \frac{(Pe-4)^2[4(2+3\eta)(343\,073 + 325\,872\eta) - 35Ca(4+\eta)(932 + 2883\eta)]}{1254\,400(2+3\eta)^2(Pe_2 - 4)}, \end{aligned}$$
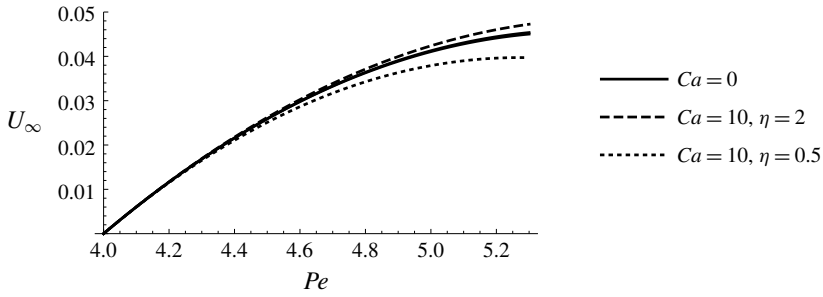$$(4.17)$$

FIGURE 4. Effect of deformability (Ca) and relative viscosity (η) on the self-propulsion velocity of an active droplet near the onset of the Marangoni instability as given in (4.17). The solid line represents the case of a non-deformable droplet ($Ca = 0$) with $\eta = 0.5$ or $\eta = 2$ (the two cases are essentially indistinguishable due to weak dependence of U_∞ on η in the limit of $Ca = 0$). The dotted and dashed lines represent deformable droplets ($Ca = 10$), with $\eta = 0.5$ and $\eta = 2$, respectively.

with $Pe_2(Ca, \eta) = [60(1 + \eta) - Ca(4 + \eta)]/(2 + 3\eta)$ (see (3.14)). One can immediately observe that at this order $\partial_{Ca} U_\infty > 0$ (respectively $\partial_{Ca} U_\infty < 0$) when $\eta > 1.0134$ (respectively $\eta < 1.0134$). The deformability of the droplet's interface therefore affects differently the self-propulsion of droplets that are more or less viscous than the surrounding fluid: roughly speaking, (4.17) states that deformability enhances self-propulsion of viscous droplets, but hinders propulsion of drops that are less viscous than the surrounding fluid (figure 4).

This result can be interpreted as follows. Steady self-propulsion of the droplet occurs when the Stokes drag balances the thrust generated by Marangoni stresses, which result from concentration gradients at the surface. In our analysis, this balance is represented by a saturated self-propelling eigenmode, where the saturation comes from nonlinear terms implementing weakly nonlinear interaction of the different components of the solution. At ϵ^3, the cumulative Marangoni stress on the drop is $\propto C_1^{(3)}(r = 1)$, see (A 2), which includes the term $\propto 1/(Pe_2 - 4)$ resulting from the interaction of the front–back symmetric component ($n = 2$) of the $O(\epsilon^2)$ concentration mode with the leading-order (i.e. $O(\epsilon)$) flow associated with self-propulsion. The second critical Péclet number Pe_2 is a decreasing function of Ca; thus increasing deformability enhances the term $\propto 1/(Pe_2 - 4)$; moreover, when $r = 1$, this term is positive (respectively negative) for $\eta < 39/29$ (respectively $\eta > 39/29$). That is, an increase in capillary number tends to increase the front–back concentration gradient of surfactant (and Marangoni forcing) for viscous droplets, while deformability tends to reduce them for less viscous droplets.

In addition, (4.13)–(4.16) establish that self-propulsion at $Ca > 0$ is always accompanied by droplet deformations of order ϵ^2 with an oblate shape, $\xi^{(2)} < 0$. Oblate deformations are known to increase the Stokes drag on a steadily moving droplet (Matunobu 1966), namely,

$$F_D \propto 1 - \epsilon^2 \xi_2^{(2)} \frac{3\eta^2 - \eta + 8}{5(1 + \eta)(2 + 3\eta)}. \tag{4.18}$$

In our case, the magnitude of droplet deformations given by $|\xi^{(2)}|$ decreases with increasing η, i.e. less viscous droplets deform more and experience higher drag and a

lower velocity for a given Marangoni forcing. Both effects of *Ca* (modified Marangoni forcing and modified viscous drag) therefore reinforce each other: drops with smaller η deform more than their viscous counterparts and, thus, experience higher drag, and they also experience a reduced Marangoni forcing, leading to the non-monotonic effect of deformability illustrated in figure 4. Interestingly, oblate deformations of active droplets were also predicted in the limit of $Pe \gg 1$ by Golovin *et al.* (1989) and in the presence of a chemical reaction in the bulk fluid by Yoshinaga (2014). An alternative approach based on reaction–diffusion equations also yields oblate deformations of the reacting domain (Shitara *et al.* 2011).

4.2. *Symmetric extensile flow (n = 2)*

The previous section focused on the analysis of the self-propelling mode of instability ($n = 1$). The present section focuses now on the second mode characterized by a symmetric extensile flow (see figure 3). In the case of $n = 2$, the solvability condition (3.14) yields $Pe = Pe_2$, and the leading-order flow is given by the second squirming mode with an unknown amplitude A_2 introduced in (3.17) and (3.18). In order to determine A_2, the solvability condition must be established for the ϵ^2 problem featuring quadratic interactions of the flow and concentration fields obtained in §3.

4.2.1. *Concentration distribution around the droplet*

For $n = 2$, $C^{(1)}(r, \mu) \propto L_2(\mu)$, and quadratic nonlinearities in (4.3) produce non-zero projections of the $O(\epsilon^2)$ concentration field onto the zeroth, second and fourth Legendre harmonics, that is,

$$C^{(2)}(r, \mu) = \sum_{n=0}^{2} C_{2n}^{(2)}(r) L_{2n}(\mu), \tag{4.19}$$

with

$$C_0^{(2)}(r) = \frac{c_0^{(2)}}{r} - Pe_2^2 A_2^2 \frac{180 - 490r + 126r^2 + 735r^3 - 630r^4}{1050r^7}$$
$$+ Pe_2 Ca A_2^2 \frac{(4 + \eta)(2 - 3r^2)}{30r^6(2 + 3\eta)}, \tag{4.20}$$

$$C_2^{(2)}(r) = \frac{c_2^{(2)}}{r^3} + \delta A_2 \frac{2 + 3r^2}{2r^4} + Pe_2 \frac{2a_{o,2}^{(2)} + 3b_{o,2}^{(2)}r^2}{2r^4} + 2Pe_2 Ca A_2^2 \frac{(4 + \eta)(1 - 3r^2)}{21r^6(2 + 3\eta)}$$
$$- Pe_2^2 A_2^2 \frac{875 - 2450r + 225r^2 + 7350r^3 + 756r^4 + 3780r^4 \log r}{3675r^7}, \tag{4.21}$$

$$C_4^{(2)}(r) = \frac{c_4^{(2)}}{r^5} + Pe_2 \frac{4a_{o,4}^{(2)} + 5b_{o,4}^{(2)}r^2}{2r^6} + 3Pe_2 Ca A_2^2 \frac{(4 + \eta)(4 + 9r^2)}{70r^6(2 + 3\eta)}$$
$$- Pe_2^2 A_2^2 \frac{2016 - 6468r + 616r^2 - 14\,553r^3 + 3564r^4 + 5544r^2 \log r}{5390r^7}, \tag{4.22}$$

where $c_n^{(2)}$ are constant amplitudes to be determined. In the absence of any translation of the droplet, the rescaled advection–diffusion equation (3.10) at ϵ^2 reduces to Laplace's equation, implying that for $n = 2$ advection of the perturbations in the far field is negligible (i.e. no boundary layer is needed here). Equivalently, it is now possible to satisfy the far-field and near-field boundary conditions for $C^{(2)}(r, \mu)$, which must decay as $r \to \infty$.

4.2.2. *Boundary and solvability conditions*

Expanding the boundary conditions (2.2) and (2.6), (2.7) up to $O(\epsilon^2)$, and substituting for $C^{(1)}$, $C^{(2)}$ and the corresponding flow field, projection of the result onto the first five Legendre polynomials provides a set of inhomogeneous linear algebraic equations for the amplitudes $a_{i,n}^{(2)}$, $b_{i,n}^{(2)}$, $a_{o,n}^{(2)}$, $b_{o,n}^{(2)}$, $c_n^{(2)}$ and $\xi_n^{(2)}$. In particular, projection of the kinematic boundary condition onto $L_0(\mu)$ yields

$$Ca\, A_2^2 \frac{6(4+\eta)}{5(2+3\eta)} = 0. \tag{4.23}$$

That is, a symmetric steady flow field around an active droplet is not possible for $Ca = O(1)$, but may exist in the limit of a weakly deformable droplet, i.e. $Ca \sim O(\epsilon)$. Indeed, a weakly deformable droplet is spherical in the leading order, $\xi^{(1)} = 0$, and features instability thresholds independent of Ca. In the particular case of $Ca \sim \epsilon$, the $O(Ca)$ terms are pushed to the next order of asymptotic expansion. For instance, the $O(Ca)$ terms in (3.2)–(3.4) appear in the corresponding boundary conditions of the problem at ϵ^2. Consequently, the solvability condition of the ϵ^2 problem is

$$A_2(49\delta(2+3\eta)^2 + 49Ca(4+\eta)(2+3\eta) + 16\,320A_2(1+\eta)^2) = 0. \tag{4.24}$$

Equation (4.24) establishes that in the limit of a weakly deformable active droplet, two branches of steady solutions exist in the ϵ-neighbourhood of Pe_2: the first branch, given by $A_2 = 0$, corresponds to a motionless state; whereas the second, featuring $A_2 < 0$, describes a symmetric extensional flow field akin to that of a force dipole. Recall that (3.18) connects the coefficient A_2 with a particular type of droplet deformation: $A_2 > 0$ (respectively $A_2 < 0$) corresponds to prolate (respectively oblate) deformations. In general, prolate and oblate deformations are not symmetric, so it is natural that our analysis yields A_2 with a particular sign.

4.3. *Simultaneous onset of the two dominant instability modes ($Pe_1 \sim Pe_2$)*

The definition of the instability thresholds (3.14) implies that for

$$Ca = 4(13 + 12\eta)/(4 + \eta) + O(\epsilon) \tag{4.25}$$

the thresholds of the first two eigenmodes coincide, namely, $|Pe_1 - Pe_2| = O(\epsilon)$. The purpose of this section is to investigate how the potential interaction of these two modes may impact the self-propulsion of the droplet. In this case, the leading-order flow field is given by the first two squirming modes with coefficients presented in (3.15)–(3.18), respectively. We now consider the problem at ϵ^2 featuring quadratic interactions of the two instability modes shown in figure 3.

The weakly nonlinear dynamics of the system is investigated in the case of

$$Ca = 4(13 + 12\eta)/(4 + \eta) + \epsilon Ca_1, \tag{4.26}$$

where the system admits two linearly independent eigenmodes and $C^{(1)}(r, \mu)$ is represented by a combination of $L_0(\mu)$, $L_1(\mu)$ and $L_2(\mu)$. Thus, at ϵ^2 quadratic nonlinearities in (4.3) produce non-zero projections onto the first five Legendre harmonics. Following the steps of the analysis presented in §§ 4.1 and 4.2, the rescaled advection–diffusion equation (3.10) reduces at ϵ^2 to (4.7) with a solution given by (4.8), and the near- and far-field solutions match in the region $\epsilon \ll \rho \ll 1$, when conditions (4.9) are met.

Expanding the boundary conditions at the droplet interface to $O(\epsilon^2)$, the projection of the kinematic boundary condition onto $L_0(\mu)$ yields

$$\frac{24(13 + 12\eta)}{5(2 + 3\eta)} A_2^2 = 0, \tag{4.27}$$

and can only be satisfied when $A_2 = 0$, as for the case of mode $n = 2$ alone, see (4.23). Consequently, the solvability condition for the problem at ϵ^2 in the case of $Pe_1 \sim Pe_2$ reads

$$A_1 = 0. \tag{4.28}$$

No non-trivial solution can be found within the $O(\epsilon)$ neighbourhood of $Pe_1 \sim Pe_2$, and in particular the regime of steady self-propulsion discussed in § 4.1 ceases to exist due to the competition between the first and the second modes of the Marangoni instability. In other words, we have arrived at a conclusion that deformability may cause a qualitative change in droplet dynamics: droplets with $Ca < 4(13 + 12\eta)/(4 + \eta)$ exhibit a regime of steady self-propulsion with $U_\infty \propto Pe - Pe_1$, whereas highly deformable drops with $Ca \geqslant 4(13 + 12\eta)/(4 + \eta)$ have no steady regime to reach in the vicinity of the base state (2.19). As demonstrated in the following section, this qualitative change in droplet behaviour can be linked to the asymptotic disparity of the time scales associated with the first two modes of the Marangoni instability.

5. Linear stability analysis and growth rates

The analysis developed so far was focused on the steady flows emerging due to saturation of neutrally stable modes. To gain further insight into the different transitions identified and the stability of each of these states (including the isotropic base state), the linear stability analysis of the system is now carried out in the vicinity of the steady solutions obtained in the previous section. We focus primarily on the linear stability of the isotropic base state (2.19), the stability of the self-propelled mode being presented in appendix B. Specifically, we obtain the growth rates of the system's eigenmodes identified in (3.15), (3.16) and (3.17), (3.18) and shown in figure 3. This analysis finally demonstrates that, near their respective instability threshold, the second instability mode grows asymptotically faster than the first one. This disparity results in fact from these modes being associated with fundamentally different physical phenomena: the first mode is intrinsically linked to the symmetry breaking of the advective boundary layer far from the droplet, whereas the second mode depends only on the interfacial dynamics of the drop.

Equations (2.1)–(2.10) are first linearized around the isotropic base state (2.19) introducing the time-dependent normal perturbations

$$(\psi_i, P_i, \psi_o, P_o)(t, r, \mu) = e^{\lambda t}(\tilde{\psi}_i, \tilde{P}_i, \tilde{\psi}_o, \tilde{P}_o)(r, \mu), \tag{5.1a}$$

$$C(t, r, \mu) = -\frac{1}{r} + e^{\lambda t}\tilde{C}(r, \mu), \quad H(t, \rho, \mu) = -\frac{\epsilon}{\rho} + e^{\lambda t}\tilde{H}(\rho, \mu), \quad \xi(t, \mu) = e^{\lambda t}\tilde{\xi}(\mu), \tag{5.1b-d}$$

where the tilde denotes the perturbations and λ is the perturbation growth rate. For simplicity, we only consider the monotonically unstable case, namely, $\lambda > 0$. Linearization for fixed values of Pe, Ca and η produces a linear eigenvalue problem for λ and the associated eigenmode $(\tilde{\psi}_i, \tilde{P}_i, \tilde{\psi}_o, \tilde{P}_o, \tilde{C}, \tilde{H}, \tilde{\xi})$. Note that this is in fact simply the generalization of (3.1)–(3.4) to the time-dependent perturbations.

As for the steady linear analysis, orthogonal eigenmodes take the form in (2.12), (2.14) and (3.5). In particular, projecting the linearized advection–diffusion equation along the first two Legendre polynomials leads to

$$\frac{\partial}{\partial r}\left(r^2\frac{\partial \tilde{C}_1}{\partial r}\right) - (Pe\,\lambda r^2 + 2)\tilde{C}_1 \;=\; 2Pe\frac{\tilde{a}_{o,1} - \tilde{b}_{o,1}r^3}{r^3}, \tag{5.2}$$

$$\frac{\partial}{\partial r}\left(r^2\frac{\partial \tilde{C}_2}{\partial r}\right) - (Pe\,\lambda r^2 + 6)\tilde{C}_2 \;=\; 6Pe\frac{\tilde{a}_{o,2} - \tilde{b}_{o,2}r^2}{r^4}, \tag{5.3}$$

where $\tilde{C}_n$ denotes the nth eigenmode of $\tilde{C}$, and $\tilde{a}_{o,1}$, $\tilde{b}_{o,1}$, $\tilde{a}_{o,2}$ and $\tilde{b}_{o,2}$ denote the amplitudes of the first two squirming modes in the expansion of $\tilde{\psi}_o$.

Unlike their steady counterparts, (5.2) and (5.3), which govern the radial component of $\tilde{C}_1$ and $\tilde{C}_2$, allow for an exponential decay of the surfactant concentration as $r \to \infty$. Therefore, there is no need to consider a far-field solution separately. Combined with the far-field boundary condition, (5.2) and (5.3) yield the following expressions for the first two eigenmodes of $\tilde{C}$:

$$\tilde{C}_1 \;=\; \tilde{c}_1 e^{-\lambda_s r}\frac{1 + \lambda_s r}{r^2} + \frac{Pe\,\tilde{a}_{o,1}}{2r^3} + \frac{2\tilde{b}_{o,1}}{\lambda r^2}$$
$$- \frac{Pe\,\lambda_s\tilde{a}_{o,1}}{8r^2}[(1 + \lambda_s r)e^{-\lambda_s r}Ei(\lambda_s r) - (1 - \lambda_s r)e^{\lambda_s r}Ei(-\lambda_s r)], \tag{5.4}$$

$$\tilde{C}_2 \;=\; \tilde{c}_2 e^{-\lambda_s r}\frac{3 + 3\lambda_s r + \lambda_s^2 r^2}{r^3} + Pe\,\tilde{a}_{o,2}\frac{8 + \lambda_s^2 r^2}{8r^4} - \frac{3Pe\,\tilde{b}_{o,2}}{4r^2} + Pe\frac{6\tilde{b}_{o,2} - \lambda_s^2\tilde{a}_{o,2}}{16\lambda_s r^3}$$
$$\times [(3 + 3\lambda_s r + \lambda_s^2 r^2)e^{-\lambda_s r}Ei(\lambda_s r) - (3 - 3\lambda_s r + \lambda_s^2 r^2)e^{\lambda_s r}Ei(-\lambda_s r)], \tag{5.5}$$

where $\lambda_s \equiv \sqrt{Pe\,\lambda}$, $Ei(x)$ denotes the exponential integral, and constants $\tilde{c}_n$ are to be determined from the boundary conditions at the droplet interface.

Substituting the eigenmodes of $\tilde{\psi}_i$, $\tilde{P}_i$, $\tilde{\psi}_o$ and $\tilde{P}_o$ along with (5.4) and (5.5) into the linearized boundary conditions (2.2), (2.6) and (2.7), two sets of linear algebraic equations are obtained. In turn, the solvability conditions of these sets determine the respective growth rate of the corresponding perturbation. In the case of the first instability mode, the solvability condition is identical to equation (14) in Michelin *et al.* (2013) and can be simplified for $|Pe - Pe_1| \ll Pe_1$ (recall that $Pe_1 = 4$, see (3.14)), resulting in the following leading-order behaviour for the growth rate of the first mode:

$$\lambda_{s,1} = \frac{3(Pe - Pe_1)}{16}. \tag{5.6}$$

Recall that we assumed $\lambda > 0$, that is, the solvability condition (5.6) holds only for $Pe > Pe_1$, where the motionless steady state becomes unstable with respect to the first mode of instability.

The solvability condition of the second instability mode is also treated asymptotically for $|Pe - Pe_2| \ll Pe_2$, with Pe_2 defined in (3.14). A different leading-order scaling is obtained this time, namely $\lambda_{s,2} \propto \sqrt{Pe - Pe_2}$, and the leading-order growth rate for the second mode near $Pe = Pe_2$ finally reads:

$$\lambda_{s,2} = \sqrt{\frac{24Pe_2(2 + 3\eta)(Pe - Pe_2)}{38\,400(1 + \eta)^2 - 4Ca(4 + \eta)(292 + 283\eta) + Ca^2(4 + \eta)(64 + 31\eta)}}. \tag{5.7}$$

Equation (5.7) holds only for $Pe > Pe_2$, when the motionless base state becomes unstable with respect to the second mode of instability.

Equations (5.6) and (5.7) imply that, near their respective thresholds, the second mode of instability grows asymptotically faster than the first one:

$$\lambda_{s,2} \gg \lambda_{s,1}. \tag{5.8}$$

This result is particularly important in the case of $Pe_1 \sim Pe_2$, when the first two instability modes are excited simultaneously. In particular, (5.8) suggests that, for $Pe_1 \sim Pe_2$, saturation of the self-propelling mode is asymptotically slower, compared to the excitation of the symmetric extensile flow associated with the second mode. We argue that the fast excitation of an unsaturated extensile flow is the reason why no non-trivial steady regimes were found in §4.3. This result also highlights the different physical nature of the first two instability modes: the self-propelling mode is associated with the symmetry breaking of the advective boundary layer far from the droplet, whereas the second mode encapsulates the interfacial dynamics of the drop.

The linear stability analysis indicates that $Pe = Pe_n$ marks a transition from the isotropic state being linearly stable ($Pe < Pe_n$) to this base state becoming unstable ($Pe > Pe_n$). For $n = 1$, this instability is associated with the onset of self-propulsion discussed in §4.1. Beyond $Pe = Pe_1$, this non-isotropic self-propelled state is itself stable to linear perturbations (see appendix B), and $Pe = Pe_1$ therefore corresponds to an exchange of stability of the two modes as expected for a transcritical bifurcation.

6. Discussion

In order to elucidate how the deformability of chemically active droplets affects the onset of their self-propulsion, the Marangoni instability of an active deformable drop submerged in surfactant solution was analysed using matched asymptotics expansions near the instability threshold. In this axisymmetric model, the instability is powered by the constant isotropic activity of the droplet (i.e. absorption of surfactant molecules to form swollen micelles) and the advection of the isotropic surfactant concentration field by the fluid motion, while the nonlinear dynamics of the model is due to both interface deformations and surfactant advection around the drop.

Two main results were obtained:

(i) Deformability was found to enhance self-propulsion of droplets that are more viscous than the surrounding medium (specifically, droplets with viscosity ratio $\eta > 1.0134$), while self-propulsion of less viscous drops ($\eta < 1.0134$) is hindered by the droplet deformability.

(ii) Deformability affects the type of bifurcation leading to symmetry breaking; in particular, moderately deformable droplets exhibit transcritical onset of self-propulsion, while in the case of highly deformable drops, our results suggest that the bifurcation becomes subcritical.

From a physical point of view, the first result (namely the increase of self-propulsion velocity for viscous deformable droplets and the reduction of the velocity for their less viscous counterparts) is the outcome of two different effects associated with the droplet deformation, which is always found to generate oblate droplets, namely an increase (respectively decrease) in hydrodynamic drag and reduction (respectively enhancement) in the front–back surfactant concentration gradient for less (respectively more) viscous droplets.

Investigation of the neutrally stable eigenmodes of the linearized problem further revealed that the interplay between surfactant advection and deformations of the droplet interface results in two competing modes of monotonic instability: the first sets in for a Péclet number above $Pe_1 \equiv 4$ and corresponds to the onset of droplet self-propulsion, whereas the second bifurcates at $Pe_2 \equiv [60(1 + \eta) - Ca(4 + \eta)]/(2 + 3\eta)$ and is characterized by a symmetric extensile flow akin to a flow driven by a force dipole. We argue that these modes reflect two different physical phenomena: the first is associated with the symmetry breaking of the advective boundary layer far from the droplet, whereas the second encapsulates the interfacial dynamics of the drop. The latter is, however, also critically relevant for the self-propulsion, as it conditions the hydrodynamic signature of the droplet, its interaction with its neighbours as well as its effect on the macroscopic stress in the fluid (Batchelor 1970; Lauga & Michelin 2016).

Above Pe_1, the motionless (isotropic) base state of the droplet (2.19) coexists with a regime of finite steady self-propulsion, whose amplitude was determined up to quadratic corrections. The base (motionless) state was observed to lose stability for $Pe > Pe_1$, while the new self-propelled mode is itself stable in that parameter range. Moreover, in the leading order, the self-propulsion velocity is $\propto Pe - 4$, suggesting that the onset of self-propulsion is a transcritical bifurcation. A similar approach was used to demonstrate that the symmetric steady flow associated with the second transition for $Pe = Pe_2$ can only exist in the case of asymptotically small capillary number, $Ca = O(\epsilon)$, i.e. in the limit of a weakly deformable droplet. Experimentally, however, it should not be possible to observe this steady (motionless) state, since in the case of $Ca = O(\epsilon)$, $Pe_1 < Pe_2$, and self-propulsion of the droplet always precedes the onset of a symmetric flow.

Deformability can nevertheless affect self-propulsion itself fundamentally: for a highly deformable droplet with $Ca = 4(13 + 12\eta)/(4 + \eta) + O(\epsilon)$, $Pe_1 \approx Pe_2$ and the two instability modes are excited simultaneously. Our results demonstrate that competition between the modes eliminates the regime of steady self-propulsion. On the other hand, we also established that steady extensile flows require $Ca = O(\epsilon)$ and, thus, are also not compatible with high droplet deformability. Consequently, in the case of $Pe_1 = Pe_2$, there are no steady flows to be found within the asymptotic limit considered in this paper. This result may be related to an asymptotic disparity in the time scales associated with the first two modes of instability. We presume that unsaturated growth of the second mode hints at a subcritical nature of the interfacial effects included in the model.

The present work therefore sheds some light on the fundamental role of deformability on the self-propulsion of active droplets. In some recent experimental studies (e.g. Izri *et al.* 2014; Moerman *et al.* 2017), the capillary number based on the droplet swimming velocity ($Ca_U = \eta U/\gamma_0$) is typically very small ($Ca_U \sim 10^{-5}$) so that the role of deformability is essentially negligible. Yet, deformability effects can become significant for systems with lower surface tension. For example, spontaneous deformation of chemically active drops due to Marangoni flows was experimentally observed in millimetre-scale oil drops with an ultra-low surface tension of roughly 0.1 mN m^{-1} by Caschera, Rasmussen & Hanczyc (2013), so that $Ca_U \sim 10^{-2}$. In this paper, we define the capillary number and dimensionless velocity based on the speed of a drop in an imposed concentration gradient (2.16), since the swimming velocity is not known *a priori*, resulting in a dimensionless terminal velocity ~ 0.01 (see figure 4). As a result $Ca \sim 100 Ca_U$ and in an experimental setting condition (4.25) corresponding to the onset of spontaneous deformations should be met when $Ca_U \sim 0.1$.

Asymptotic methods provide significant insight into the interplay of several key physical mechanisms in the dynamics of active droplets, such as surfactant advection by the Marangoni flows or droplet deformation. Consequently, the present study is intrinsically limited to the immediate vicinity of the instability threshold and does not rule out further bifurcations in the dynamical behaviour of such active droplets, which require further investigation.

Our findings indicate that the bifurcation structure of steady flows around an active droplet depends on the value of capillary number, which quantifies droplet deformability. In that regard, capillary number may be seen as a control parameter: setting the value of Ca determines the nature of the corresponding symmetry-breaking bifurcation. We conjecture that the effect of deformability on the dynamics of chemically driven self-propulsion might be relevant in the context of biology. Indeed, chemically active droplets are widely used to model the behaviour of cells (Nagasaka *et al.* 2017) and it is well established that cells do change their elastic properties dynamically to enhance adhesion and facilitate cell sorting (Winklbauer 2015). Further investigation is thus necessary to elucidate the specific role that deformability plays in cell dynamics.

Acknowledgement

Appendix A. Details of the $O(\epsilon^3)$ solution

In the near field, surfactant concentration is given by a superposition of Legendre polynomials, $C^{(3)}(r, \mu) = \sum_{n=0}^{3} C_n^{(3)}(r) L_n(\mu)$, with

$$C_0^{(3)}(r) = \frac{c_0^{(3)}}{r} + d_0^{(3)} - \delta B_1 \frac{8 - 15r + 20r^3 + 80r^6}{120r^5} - \delta^3 \frac{16 - 35r + 40r^3 + 160r^6 - 20r^7}{30\,720r^5}, \tag{A 1}$$

$$\begin{aligned}
C_1^{(3)}(r) = {}& \frac{c_1^{(3)}}{r^2} + d_1^{(3)}r + \delta B_1 \frac{1 + 2r^3}{2r^3} \\
&+ 3\delta^3 \frac{3 - 7r + 12r^2 + 20r^3 + 28r^4 + 56r^6 + 84r^7 + 56r^9}{143\,360r^7} \\
&+ \frac{33\delta^3}{627\,200r^6(Pe_2 - 4)} \left(115 - 35r\frac{24 + 31\eta}{2 + 3\eta} + 21r^2 + 455r^3 - 210r^5 \right), \tag{A 2}
\end{aligned}$$

$$\begin{aligned}
C_2^{(3)}(r) = {}& \frac{c_2^{(3)}}{r^3} + d_2^{(3)}r^2 - \delta B_1 \frac{10 - 21r + 70r^3 - 42r^4 + 28r^6}{84r^5} \\
&- \delta^3 \frac{20 - 49r + 140r^3 - 112r^4 + 56r^6}{21\,504r^5} - 33\delta^3 \frac{2 + 3r^2}{1792r^4(Pe_2 - 4)}, \tag{A 3}
\end{aligned}$$

$$\begin{aligned}
C_3^{(3)}(r) = {}& \frac{c_3^{(3)}}{r^4} + d_3^{(3)}r^3 + \delta^3 \frac{8 - 21r + 81r^2 - 126r^4 + 162r^5 + 168r^6 - 63r^7 + 28r^9}{215\,040r^5} \\
&+ \frac{11\delta^3}{1756\,160r^6(Pe_2 - 4)} \left(1274 - 441r\frac{24 + 31\eta}{2 + 3\eta} + 216r^2 + 1512r^2 \log r \right. \\
&\left. + 2058r^3 - 1764r^4\frac{9 + 11\eta}{2 + 3\eta} + 1764r^5 \right), \tag{A 4}
\end{aligned}$$

where $c_n^{(3)}$ and $d_n^{(3)}$ are unknown constant amplitudes to be determined in the matching process with the far-field boundary layer.

The far-field solution can be written as

$$
\begin{aligned}
H^{(3)}(\rho, \mu) = {}& e^{-\rho_s(1+\mu)} \left(-\frac{\delta^3 \rho_s}{192} + \delta B_1 \frac{3 + 6\rho_s - 8\rho_s^2}{6\rho_s} - \frac{256\rho_s B_1^2}{3\delta} + 2b_{o,1}^{(3)} \frac{1 + 2\rho_s}{\rho_s} \right. \\
& + \frac{\mu}{256\delta\rho_s^2} [\delta^4(3 + 3\rho_s - 2\rho_s^3) + 128\delta^2 B_1(9 + 9\rho_s + 2\rho_s^2 - 4\rho_s^3) \\
& \times 2 + 16\,384 B_1^2(3 + 3\rho_s - 2\rho_s^3) + 512\delta_s b_{o,1}^{(3)}(3 + 3\rho_s + 2\rho_s^2)] \\
& \left. + L_2(\mu) \frac{(\delta^2 + 128 B_1)^2(45 + 45\rho_s + 15\rho_s^2 - 2\rho_s^4)}{768\delta\rho_s^3} \right) \\
& + \frac{e^{-\rho_s\mu}}{\sqrt{\rho_s}} \sum_{n=0}^{\infty} h_n^{(3)} K_{n+1/2}(\rho_s) L_n(\mu),
\end{aligned}
\tag{A 5}
$$

where $h_n^{(3)}$ are unknown constant amplitudes and $\rho_s \equiv Pe_1 A_1 \rho = \delta\rho/8 \geqslant 0$.

Matching of near- and far-field surfactant concentrations (A 1)–(A 5), and subsequent substitution of the result into the boundary conditions (2.2), (2.6) and (2.7) expanded at $O(\epsilon^3)$ yields the solvability condition of the cubic problem providing a correction to the droplet self-propulsion velocity (4.17).

Appendix B. Linear stability analysis of the steady state featuring self-propulsion

As a complement to the linear stability analysis of the isotropic base state near Pe_1 obtained in §4.1, the stability of the non-trivial self-propelled mode obtained for $Pe \geqslant Pe_1$ is now investigated, in order to demonstrate further that the onset of self-propulsion is a transcritical bifurcation.

As in §5, infinitesimal normal perturbations of the anisotropic state are introduced:

$$
\psi_i(t, r, \mu) = \epsilon\delta \frac{3r^2(1 - r^2)(1 - \mu^2)}{64} + e^{\lambda t} \tilde{\psi}_i(r, \mu),
\tag{B 1}
$$

$$
P_i(t, r, \mu) = -\epsilon\delta \frac{4(2 + 3\eta) + 15r\mu}{16\eta} + e^{\lambda t} \tilde{P}_i(r, \mu),
\tag{B 2}
$$

$$
\psi_o(t, r, \mu) = \epsilon\delta \frac{(1 - r^3)(1 - \mu^2)}{32r} + e^{\lambda t} \tilde{\psi}_o(r, \mu),
\tag{B 3}
$$

$$
P_o(t, r, \mu) = e^{\lambda t} \tilde{P}_i(r, \mu), \quad \xi(t, \mu) = e^{\lambda t} \tilde{\xi}(\mu),
\tag{B 4a,b}
$$

$$
C(t, r, \mu) = -\frac{1}{r} + \frac{\epsilon\delta}{8} \left(1 + \mu + \mu \frac{2 - 3r}{4r^3} \right) + e^{\lambda t} \tilde{C}(r, \mu),
\tag{B 5}
$$

$$
H(t, \rho, \mu) = -\frac{\epsilon}{\rho} e^{-\delta\rho(1+\mu)/8} + e^{\lambda t} \tilde{H}(\rho, \mu),
\tag{B 6}
$$

where the tilde denotes the perturbations, and λ is the perturbation growth rate. Similarly to §5, we focus on the monotonically unstable case, where $\lambda > 0$. Using (B 1)–(B 5), the full nonlinear system (2.1)–(2.10) is linearized around the self-propelling state with respect to perturbations, thus obtaining a linear eigenvalue problem for λ the associated eigenvector $(\tilde{\psi}_i, \tilde{P}_i, \tilde{\psi}_o, \tilde{P}_o, \tilde{C}, \tilde{H}, \tilde{\xi})$. This problem is

tractable within the framework of the matched asymptotic expansions employed in §§ 3 and 4 when λ is of the form

$$\lambda = \epsilon^2 \lambda^{(1)} + \epsilon^3 \lambda^{(2)} + \cdots, \tag{B 7}$$

and the corresponding eigenvector is expanded as $\tilde{f} = f^{(1)} + \epsilon f^{(2)} + \cdots$, with f being any component of the eigenvector above. As a result, a sequence of linear problems at $\epsilon^0, \epsilon^1, \ldots$ is obtained, where each of the problems in the sequence represents a Stokes flow past a liquid sphere.

B.1. *Leading-order problem*

The leading-order problem is first analysed. In essence, we apply the algorithm described in § 3 to the linearized problem at ϵ^0. At ϵ^0, the linearized advection–diffusion equation is identical to (3.1), and $\tilde{C}^{(1)}$ is therefore given by (3.5), (3.6) and (3.7) – with potentially different constants $c_n^{(1)}$ and $d_n^{(1)}$ in comparison with § 3. The far-field solution is then obtained as

$$\tilde{H}^{(1)}(\rho, \mu) = \frac{b_{o,1}^{(1)} e^{-\delta\rho(1+\mu)/8}}{4\lambda^{(1)}} \left(\frac{\delta}{\rho} + \mu \frac{8 + \delta\rho}{\rho^2} \right) + \frac{e^{-\delta\rho\mu/8}}{\sqrt{\rho}} \sum_{n=0}^{\infty} h_n^{(1)} K_{n+1/2}(q\rho/8) L_n(\mu), \tag{B 8}$$

where $q \equiv \sqrt{\delta^2 + 256\lambda^{(1)}}$. After matching the near- and far-field solutions, we solve the set of algebraic equations emerging from the boundary conditions at the droplet interface. For the self-propelling mode, the solution of the leading-order problem for the perturbations reads

$$b_{i,0}^{(1)} = \frac{4A_1}{3\eta}(2 + 3\eta), \quad \frac{3}{2}a_{i,1}^{(1)} = \frac{3}{2}b_{i,1}^{(1)} = a_{o,1}^{(1)} = b_{o,1}^{(1)} = A_1, \tag{B 9a,b}$$

$$c_0^{(1)} = 0, \quad d_0^{(1)} = \delta A_1 \frac{q - \delta}{32\lambda^{(1)}}, \quad c_1^{(1)} = -3A_1, \quad d_1^{(1)} = 0, \tag{B 10a–d}$$

where $q \equiv \sqrt{\delta^2 + 256\lambda^{(1)}}$ and an unknown constant A_1 will be determined from the solvability condition at $O(\epsilon)$. Solution (B 9)–(B 10) is almost identical to the solution of the linearized steady problem (3.15)–(3.16), with the exception of the coefficient $d_0^{(1)}$ corresponding to the isotropic perturbation of the surfactant concentration. It is easy to see that, in the case of positive perturbation growth rate, $\lambda > 0$, coefficient $d_0^{(1)}$ carries the information about the growth rate to the next order of expansion.

B.2. *Problem at ϵ*

Turning now to the $O(\epsilon)$ problem for the perturbations around the self-propelled steady state, we repeat the steps of the analysis developed in § 4.1. First, we obtain the solution of the near-field advection–diffusion equation, $\tilde{C}^{(2)}(r, \mu) = \sum_{n=0}^{2} \tilde{C}_n^{(2)}(r) L_n(\mu)$, where

$$\tilde{C}_0^{(2)}(r) = \frac{c_0^{(2)}}{r} + d_0^{(2)} - \delta\tilde{A}_1 \left(\frac{2r}{3} + \frac{1}{6r^2} - \frac{1}{8r^4} + \frac{1}{15r^5} \right), \tag{B 11}$$

$$\tilde{C}_1^{(2)}(r) = \frac{c_1^{(2)}}{r^2} + d_1^{(2)}r + \delta\tilde{A}_1 \frac{1 + 2r^3}{2r^3} + \frac{2a_{o,1}^{(2)} + 4b_{o,1}^{(2)}r^3}{r^3}, \tag{B 12}$$

$$\tilde{C}_2^{(2)}(r) = \frac{c_2^{(2)}}{r^3} + d_2^{(2)} r^2 + \frac{4a_{o,2}^{(2)} + 6b_{o,2}^{(2)} r^2}{r^4} - \delta \tilde{A}_1 \left(\frac{r}{3} - \frac{1}{2r} + \frac{5}{6r^2} - \frac{1}{4r^4} + \frac{5}{42r^5} \right).$$
(B 13)

Then the far-field solution is obtained as

$$\begin{aligned}
\tilde{H}^{(2)}(\rho, \mu) = {} & \frac{\tilde{A}_1 e^{-\rho(q+\delta\mu)/8}}{\lambda^{(1)}} \left(\delta \frac{\delta^3 + 160\delta\lambda^{(1)} + 384\lambda^{(2)}}{96q} \right. \\
& \left. + \frac{\mu}{64}(\delta^3 + 64\delta\lambda^{(1)} + 256\lambda^{(2)}) + \delta^2 L_2(\mu) \frac{8 + q\rho}{192\rho} \right) \\
& - \frac{\tilde{A}_1 e^{-\delta\rho(1+\mu)/8}}{3Pe_1(\lambda^{(1)})^2} \left(\delta \frac{\delta^3 + 96\delta\lambda^{(1)} + 384Pe_1\lambda^{(2)}}{384\rho} \right. \\
& \left. + \mu(\delta^3 + 64\delta\lambda^{(1)} + 256\lambda^{(2)}) \frac{8 + \delta\rho}{256\rho^2} + \delta^2 L_2(\mu) \frac{192 + 24\delta\rho + \delta^2\rho^2}{768\rho^3} \right) \\
& + \frac{4b_{o,1}^{(2)} + \delta\tilde{A}_1}{16\lambda^{(1)}} e^{-\delta\rho(1+\mu)/8} \left(\frac{\delta}{\rho} + \mu \frac{8 + \delta\rho}{\rho^2} \right) \\
& + \frac{e^{-\delta\rho\mu/8}}{\sqrt{\rho}} \sum_{n=0}^{\infty} h_n^{(2)} K_{n+1/2}(q\rho/8) L_n(\mu).
\end{aligned}$$
(B 14)

Finally, we match near- and far-field solutions and use the boundary conditions at the droplet interface (2.2), (2.6) and (2.7) for the perturbation fields evaluated up to $O(\epsilon)$ to obtain the solvability condition of the problem at ϵ, which reads

$$Ca^2(Pe_1 - Pe_2)(2q^2 - \delta q + 5\delta^2) = 0.$$
(B 15)

It is easy to see that (B 15) is satisfied only when $Ca = O(\epsilon)$. Indeed, the limit of $Pe_1 = Pe_2$ is degenerate, since the steady self-propelling regime ceases to exist, while (B 15) has no real solution for q above the instability threshold, $Pe > Pe_1$ (recall that a self-propelling steady state does not exist for $Pe < Pe_1$).

We repeat the solution of the $O(\epsilon)$ problem for the perturbations of the self-propelled steady state in the limit of a weakly deformable droplet, $Ca = \epsilon Ca_1$. In this case, the near- and far-field solutions remain the same as in the case of finite capillary number, while the solvability condition can be written as

$$Ca_1(q^2 - 2\delta q + \delta^2) = 0.$$
(B 16)

Again, (B 16) has no real solutions for q above the instability threshold, $Pe > Pe_1$, and thus can be satisfied only when $Ca_1 \ll \epsilon$.

Repeating the solution of the $O(\epsilon)$ problem in the limit of non-deformable droplet, $Ca = 0$, yields near- and far-field solutions given by (B 11)–(B 14) and the following solvability condition

$$2q^2 - \delta q + 5\delta^2 = 0.$$
(B 17)

Similarly to the solvability conditions (B 15) and (B 16), (B 17) has no real solutions for q above the instability threshold, $Pe > Pe_1$. Finally, we combine solvability conditions (B 15)–(B 17) and establish that the perturbation growth rate $\lambda^{(1)}$ is strictly negative and the steady state featuring self-propulsion is stable for $Pe > Pe_1$.

REFERENCES

ACRIVOS, A. & TAYLOR, T. D. 1962 Heat and mass transfer from single spheres in Stokes flow. *Phys. Fluids* **5**, 387–394.

ANDERSON, J. L. 1989 Colloid transport by interfacial forces. *Annu. Rev. Fluid Mech.* **21**, 61–99.

BARET, J. F. 1969 Theoretical model for an interface allowing a kinetic study of adsorption. *J. Colloid Interface Sci.* **30**, 1–12.

BATCHELOR, G. K. 1970 The stress system in a suspension of force-free particles. *J. Fluid Mech.* **41**, 545–570.

BLAKE, J. R. 1971 A spherical envelope approach to ciliary propulsion. *J. Fluid Mech.* **46**, 199–208.

CASCHERA, F., RASMUSSEN, S. & HANCZYC, M. M. 2013 An oil droplet division–fusion cycle. *ChemPlusChem* **78**, 52–54.

FADDA, F., GONNELLA, G., LAMURA, A. & TIRIBOCCHI, A. 2017 Lattice Boltzmann study of chemically-driven self-propelled droplets. *Eur. Phys. J.* E **40** (12), 112.

FRENKEL, M., DOMBROVSKY, L., MULTANEN, V., DANCHUK, V., LEGCHENKOVA, I., SHOVAL, S., BORMASHENKO, Y., BINKS, B. P. & BORMASHENKO, E. 2018 Self-propulsion of water-supported liquid marbles filled with sulfuric acid. *J. Phys. Chem.* B **122**, 7936–7942.

GOLOVIN, A. A., GUPALO, Y. P. & RYAZANTSEV, Y. S. 1989 Change in shape of drop moving due to the chemithermocapillary effect. *J. Appl. Mech. Tech. Phys.* **30**, 602–609.

HAPPEL, J. & BRENNER, H. 1983 *Low Reynolds Number Hydrodynamics: With Special Applications to Particulate Media (Mechanics of Fluids and Transport Processes)*. Springer.

HERMINGHAUS, S., MAASS, C. C., KRÜGER, C., THUTUPALLI, S., GOEHRING, L. & BAHR, C. 2014 Interfacial mechanisms in active emulsions. *Soft Matt.* **10**, 7008–7022.

HOLMES, M. H. 1995 *Introduction to Perturbation Methods*. Springer.

IBRAHIM, Y., GOLESTANIAN, R. & LIVERPOOL, T. B. 2018 Shape dependent phoretic propulsion of slender active particles. *Phys. Rev. Fluids* **3**, 033101.

IZRI, Z., VAN DER LINDEN, M. N., MICHELIN, S. & DAUCHOT, O. 2014 Self-propulsion of pure water droplets by spontaneous Marangoni-stress-driven motion. *Phys. Rev. Lett.* **113**, 248302.

JIN, C., HOKMABAD, B. V., BALDWIN, K. A. & MAASS, C. C. 2018 Chemotactic droplet swimmers in complex geometries. *J. Phys.: Condens. Matter* **30**, 054003.

KREE, R., BURADA, P. S. & ZIPPELIUS, A. 2017 From active stresses and forces to self-propulsion of droplets. *J. Fluid Mech.* **821**, 595–623.

KRÜGER, C., BAHR, C., HERMINGHAUS, S. & MAASS, C. C. 2016a Dimensionality matters in the collective behaviour of active emulsions. *Eur. Phys. J.* E **39**, 64–72.

KRÜGER, C., KLÖS, G., BAHR, C. & MAASS, C. C. 2016b Curling liquid crystal microswimmers: a cascade of spontaneous symmetry breaking. *Phys. Rev. Lett.* **117**, 048003.

LAMB, H. 1945 *Hydrodynamics*, Dover Books on Physics. Dover.

LAUGA, E. & MICHELIN, S. 2016 Stresslets induced by active swimmers. *Phys. Rev. Lett.* **117**, 148001.

LEAL, L. G. 2007 *Advanced Transport Phenomena: Fluid Mechanics and Convective Transport Processes*, Cambridge Series in Chemical Engineering. Cambridge University Press.

MAASS, C. C., KRÜGER, C., HERMINGHAUS, S. & BAHR, C. 2016 Swimming droplets. *Annu. Rev. Condens. Matter Phys.* **7**, 171–193.

MATUNOBU, Y. 1966 Motion of a deformed drop in Stokes flow. *J. Phys. Soc. Japan* **21**, 1596–1602.

MICHELIN, S. & LAUGA, E. 2015 Autophoretic locomotion from geometric asymmetry. *Eur. Phys. J.* E **38**, 7.

MICHELIN, S. & LAUGA, E. 2017 Geometric tuning of self-propulsion for Janus catalytic particles. *Sci. Rep.* **7**, 42264.

MICHELIN, S., LAUGA, E. & BARTOLO, D. 2013 Spontaneous autophoretic motion of isotropic particles. *Phys. Fluids.* **25**, 061701.

MOERMAN, P. G., MOYSES, H. W., VAN DER WEE, E. B., GRIE, D. G., VAN BLAADEREN, A., KEGEL, W. K., GROENEWOLD, J. & BRUJIC, J. 2017 Solute-mediated interactions between active droplets. *Phys. Rev.* E **96**, 032607.

MORAN, J. L. & POSNER, J. D. 2017 Phoretic self-propulsion. *Annu. Rev. Fluid Mech.* **49**, 511–540.

NAGASAKA, Y., TANAKA, S., NEHIRAA, T. & AMIMOTO, T. 2017 Spontaneous emulsification and self-propulsion of oil droplets induced by the synthesis of amino acid-based surfactants. *Soft Matt.* **13**, 6450–6457.

NOURHANI, A. & LAMMERT, P. E. 2016 Geometrical performance of self-propelled colloids and microswimmers. *Phys. Rev. Lett.* **116**, 178302.

OHTA, T. 2017 Dynamics of deformable active particles. *J. Phys. Soc. Japan* **86**, 072001.

REDNIKOV, A. YE., RYAZANTSEV, Y. S. & VELARDE, M. G. 1994*a* Active drops and drop motions due to nonequilibrium phenomena. *J. Non-Equilib. Thermodyn.* **19**, 95–113.

REDNIKOV, A. YE., RYAZANTSEV, Y. S. & VELARDE, M. G. 1994*b* Drop motion with surfactant transfer in a homogeneous surrounding. *Phys. Fluids* **6**, 451–468.

RYAZANTSEV, Y. S., VELARDE, M. G., RUBIO, R. G., ORTEGA, F. & LÓPEZ, P. 2017 Thermo- and soluto-capillarity: passive and active drops. *Adv. Colloid Interface Sci.* **247**, 52–80.

SCHMITT, M. & STARK, H. 2013 Swimming active droplet: a theoretical analysis. *Europhys. Lett.* **101**, 44008.

SCHMITT, M. & STARK, H. 2016 Marangoni flow at droplet interfaces: three-dimensional solution and applications. *Phys. Fluids* **28**, 012106.

SHITARA, K., HIRAIWA, T. & OHTA, T. 2011 Deformable self-propelled domain in an excitable reaction–diffusion system in three dimensions. *Phys. Rev.* E **83**, 066208.

SHKLYAEV, S., BRADY, J. F. & CORDOVA-FIGUEROA, U. M. 2014 Non-spherical osmotic motor: chemical sailing. *J. Fluid Mech.* **748**, 488–520.

SUGA, M., SUDA, S., ICHIKAWA, M. & KIMURA, Y. 2018 Self-propelled motion switching in nematic liquid crystal droplets in aqueous surfactant solutions. *Phys. Rev.* E **97**, 062703.

THUTUPALLI, S., SEEMANN, R. & HERMINGHAUS, S. 2011 Swarming behavior of simple model squirmers. *New J. Phys.* **13**, 073021.

WEBER, C. A., ZWICKER, D., JÜLICHER, F. & LEE, C. F. 2018 Physics of active emulsions. arXiv:1806.09552.

WINKLBAUER, R. 2015 Cell adhesion strength from cortical tension an integration of concepts. *J. Cell Sci.* **128**, 3687–3693.

WÜRGER, A. 2014 Thermally driven Marangoni surfers. *J. Fluid Mech.* **752**, 589–601.

YABUNAKA, S., OHTA, T. & YOSHINAGA, N. 2012 Self-propelled motion of a fluid droplet under chemical reaction. *J. Chem. Phys.* **136**, 074904.

YABUNAKA, S. & YOSHINAGA, N. 2016 Collision between chemically driven self-propelled drops. *J. Fluid Mech.* **806**, 205–233.

YARIV, E. & KAYNAN, U. 2017 Phoretic drag reduction of chemically active homogeneous spheres under force fields and shear flows. *Phys. Rev. Fluids* **2**, 012201(R).

YOSHINAGA, N. 2014 Spontaneous motion and deformation of a self-propelled droplet. *Phys. Rev.* E **89**, 012913.

YOSHINAGA, N. 2017 Simple models of self-propelled colloids and liquid drops: from individual motion to collective behaviors. *J. Phys. Soc. Japan* **86**, 101009.

YOSHINAGA, N., NAGAI, K. N., SUMINO, Y. & KITAHATA, H. 2012 Drift instability in the motion of a fluid droplet with a chemically reactive surface driven by Marangoni flow. *Phys. Rev.* E **86**, 016108.